Monthly Notices
of the
ROYAL ASTRONOMICAL SOCIETY

MNRAS **493,** 3473–3489 (2020) doi:10.1093/mnras/staa517

Characterizing low-contrast Galactic open clusters with *Gaia* Data Release 2

M. S. Angelo [1]★ J. F. C. Santos Jr [2,3] and W. J. B. Corradi[2,4]

[1] *Centro Federal de Educação Tecnológica de Minas Gerais, Av. Monsenhor Luiz de Gonzaga, 103, 37250-000 Nepomuceno, MG, Brazil*
[2] *Departamento de Física, ICEx, Universidade Federal de Minas Gerais, Av. Antônio Carlos 6627, 31270-901 Belo Horizonte, MG, Brazil*
[3] *Departamento de Astronomía, Universidad La Serena, Av. Juan Cisternas 1200, La Serena, Chile*
[4] *Laboratório Nacional de Astrofísica, R. Estados Unidos 154, 37530-000 Itajubá, MG, Brazil*

Accepted 2020 February 14. Received 2020 February 14; in original form 2019 December 31

ABSTRACT

In this study, we characterized 16 objects previously classified as faint or low-contrast Galactic open clusters (OCs). We employed parameters associated with the dynamical evolution of the OCs: the core (r_c), tidal (r_t) and half-mass (r_{hm}) radii, age and crossing time (t_{cr}). Relations among these parameters were exploited to draw some evolutionary connections. We also included 11 OCs with previous characterizations to provide wider coverage of the parameter space. The investigated sample spans a considerable range in age, $\log(t\ \mathrm{yr}^{-1})$ ∼7.0–9.7, and Galactocentric distance, $R_G \sim$ 6–11 kpc). Most of these OCs present solar metallicity. We employed *Gaia* Data Release 2 astrometry and photometry, and we selected member stars through a decontamination algorithm that explores the three-dimensional astrometric space ($\mu_\alpha, \mu_\delta, \varpi$) to assign membership likelihoods. Previous studies of most of these objects were based mostly on photometric information. All investigated OCs were proved to be real stellar concentrations. The relations among their parameters indicate a general disruption scenario in which OCs tend to be more concentrated as they evolve. Internal interactions sucessively drive OCs to develop more dynamically relaxed structures and make them less subject to mass loss due to tidal effects. Tidal radius tends to increase with R_G in accordance with the strength of the Galactic tidal field. Besides, the correlation between r_c and the dynamical ratio $\tau_{dyn} =$ age/t_{cr} suggests two distinct evolutionary sequences, which may be a consequence of different initial formation conditions.

Key words: technique: photometric – open clusters and associations: general.

1 INTRODUCTION

It is particularly challenging to investigate open clusters (OCs) that present a low stellar density contrast against the Galactic disc field population. There are a number of reasons why OCs might be barely distinguishable from the field: (i) they can be projected against a very dense stellar background (e.g. Ferreira et al. 2019); (ii) they can be severely obscured by interstellar absorption (e.g. Bianchin et al. 2019); (iii) they can be intrinsically poorly populated (e.g. Pavani et al. 2011; Angelo et al. 2019a) due to the loss of stars during their dynamical evolution.

In this context, the publication of high-precision astrometric and photometric data available in the *Gaia* Data Release 2 (DR2) catalogue (Katz et al. 2018) has inaugurated a new era in astronomy. The use of such data allows us to circumvent the difficulties arising mainly from points (i) and (iii) above, because the search for a statistically significant concentration of stars in the astrometric space can be used to unambigously distinguish cluster populations from field populations. This strategy has led to an increase in the number of OCs discovered and it has also allowed more precise characterization of already known OCs (e.g. Cantat-Gaudin et al. 2018a; Castro-Ginard et al. 2018; Ferreira et al. 2019; Monteiro & Dias 2019). For OCs strongly affected by interstellar extinction, the *Gaia* visible bands are of limited help, and studies of this type of object usually require an analysis in conjunction with longer wavelengths.

In the last decade, an effort has been made to construct data bases compiling lists of OCs and their fundamental parameters. Two of these are WEBDA (Netopil, Paunzen & Stütz 2012), containing ∼1200 clusters, and DAML02 (Dias et al. 2002; version 3.5 as of 2016 January), containing ∼2200 clusters. Kharchenko et al. (2013) determined structural, kinematic and astrophysical parameters for ∼3000 OCs and associations with the use of an automatic pipeline, which works on proper motions and near-infrared photometric data collected from the PPMXL (Roeser, Demleitner & Schilbach 2010)

★ E-mail: mateusangelo@cefetmg.br

and Two-Micron All-Sky Survey (2MASS; Skrutskie et al. 2006) catalogues, respectively. More recently, Bica et al. (2019) presented a catalogue of Galactic star clusters, associations and candidates, with 10 978 entries. For the construction of this multiband catalogue, both large and small catalogues were analysed, together with small-sample papers. These catalogues are in general related to specific surveys, such as the ESO Visible and Infrared Survey Telescope for Astronomy (VISTA) Variables in the Vía Láctea (VVV) survey (Minniti et al. 2010), the UKIRT Infrared Deep Sky Survey (UKIDSS; Lawrence et al. 2007), the *Wide-field Infrared Survey Explorer* (*WISE*; Cutri et al. 2012) and 2MASS.

To date, about 3200 objects have measured parameters in the literature and a very limited number of objects have been studied with some detail from a dynamical point of view (e.g. Piskunov et al. 2007; Piatti, Dias & Sampedro 2017; Angelo et al. 2019b). Complete characterizations of OCs, including not only fundamental parameters (such as age, distance and interstellar reddening) but also structural and kinematic information, are fundamental for a deeper understanding of the structure, formation and evolution of the Galactic disc (Dias et al. 2019). Besides, they provide observational constraints for *N*-body simulations aimed at describing the cluster evolution (e.g. Rossi, Bekki & Hurley 2016; Reina-Campos et al. 2019).

The present study is a contribution to increase the number of dynamically investigated objects. Here, we focus on a non-exhaustive list of 16 OCs previously classified as low-contrast or faint objects, in general highly field-contaminated and/or poorly-populated. Some of them were indicated as asterisms in previous studies (Section 4.3). Previous analysis of these objects (Bica & Bonatto 2005, 2011; Bica, Bonato & Blumberg 2006) employed 2MASS photometry and a decontamination tool applied to these clusters' colour–magnitude diagrams (CMDs) in order to determine their physical nature (as real OCs or asterisms). In the present paper, we revisited the analysis of these objects, this time taking full advantage of high-precision *Gaia* DR2 photometry and astrometry, which allowed more refined lists of member stars. Cleaned CMDs (Section 3) were obtained after applying a decontamination algorithm that looks for significant overdensities in the astrometric space and assigns membership likelihoods. Because some important discrepancies have been found between our derived parameters and those in the literature, we propose that the properties of these OCs should be revised. In Section 4.2, we compared our results for a subsample in common with Cantat-Gaudin et al. (2018b).

This paper is organized as follows. in Section 2, we present the investigated sample and the collected data. In Section 3, we present our analysis method. The results are shown in Section 4 and discussed in Section 5, where we characterize the evolutionary stages of the OCs by employing parameters associated with their dynamical evolution: the core (r_c), tidal (r_t) and half-mass (r_{hm}) radii, age and crossing time (t_{cr}). Relations between these parameters are exploited to draw some evolutionary connections. Section 6 summarizes our main conclusions.

2 DATA

Sixteen objects in our sample were taken from the lists of Bica & Bonatto (2005, 2011) and Bica et al. (2006), where they were classified as faint or low-contrast Galactic OCs. In order to enlarge our sample and to provide a wider domain of the investigated dynamical parameters, we complemented our sample with another 11 OCs with previous characterizations in the literature. The list of investigated objects and the whole set of structural and fundamental parameters (as determined according to the procedures stated in Section 3) are shown in Tables 1 and 2.

In all cases, we employed the Vizier tool[1] to extract astrometric and photometric data from the *Gaia* DR2 catalogue within ∼1° of the objects' central coordinates as listed in DAML02. In order to ensure good quality of the astrometric information, we limited the whole set of data to those stars that are consistent with equations (1) and (2) of Arenou et al. (2018), aiming at excluding spurious data.

3 METHOD

3.1 Pre-analysis: finding the signature of a cluster

In the first step of our analysis, we searched for signals of the physical existence of the investigated clusters by inspecting the dispersion of data in their CMDs and vector-point diagrams (VPDs), previously to the application of the decontamination method described in Section 3.3.

After applying the basic filtering process, as stated in the previous section, we restricted the data of each cluster to a squared area with a size of at least four times the limiting radius (R_{lim}), as informed in DAML02. The procedure is ilustrated in Fig. 1 for the case of King 20. We can note a low-contrast concentration of bright stars in the central part of its skymap (40×40 arcmin^2 field of view) projected against a dense stellar background ($b \sim -3°$). The left panel of Fig. 2 shows the corresponding CMD. We took proper motions for stars with $G \leq 18$ mag (filled circles in the CMD) and built the VPD for them, as shown in the right panel of Fig. 2.

This filtering process revealed a conspicuous concentration of stars around $(\mu_\alpha \cos\delta, \mu_\delta) \sim (-2.6, -2.6)$ mas yr^{-1}. It would be difficult to verify the existence of such groups of stars without the magnitude filter, due to large field contamination mainly by faint disc stars. In order to alleviate the field contamination and thus improve the determination of the cluster's structural parameters (Section 3.2), we took stars within a squared box with side 2 mas yr^{-1} centred on the main group (green rectangle in Fig. 2). This box size is large enough to encompass the member stars without a significant field contamination. The final result of this set of filtering processes is shown in the right panel of Fig. 1, where the presence of the cluster can be clearly verified. Analogous procedures were employed for the whole sample of investigated OCs. When a clear overdensity in the VPDs could not be obtained, we restricted the cluster's skymap to squared areas of ∼two times the literature value of R_{lim} and/or applied more restrictive magnitude filters, typically keeping those stars in the range $G \leq 17$ mag.

3.2 Structural parameters

The second step in our analysis was to determine the clusters' central coordinates and structural parameters: the core (r_c), tidal (r_t) and half-mass (r_{hm}) radii. To accomplish this, we restricted each cluster to a subsample of stars consistent with the CMD and VPD filters (i.e., magnitude cuts and proper motions box, as defined in the previous section), in order to provide better contrasts between cluster and field populations. To refine the central coordinates, we built a grid of evenly spaced ($\Delta \sim 0.5$ arcmin) α, δ pairs centred on the literature values (DAML02). At least ∼200 pairs were employed during this step. Each α, δ pair was treated as a tentative centre, for which we built radial density profiles (RDPs) by counting the

[1] See http://vizier.u-strasbg.fr/viz-bin/VizieR.

Table 1. Redetermined central coordinates, Galactocentric distances and structural parameters of the studied OCs. To convert arcmin into pc we used the expression $r(\mathrm{pc}) = r(\mathrm{arcmin}) \times (\pi/10\,800) \times 10^{[(m-M)_0+5]/5}$, where $(m-M)_0$ is the OC distance modulus (see Table 2). Note that 14 of the 16 OCs in the main sample were previously investigated by Bica & Bonatto (2005, 2011) and Bica et al. (2006). The OCs NGC 2421 and [FSR2007] 1325 were included as they are projected in the same regions of Czernik 31 and Czernik 32, respectively (see Section 4.3)

Cluster	RA (h:m:s)	Dec. (°:′:″)	ℓ (°)	b (°)	R_G[a] (kpc)	r_c (pc)	r_{hm} (pc)	r_t (pc)
				Main sample				
Haffner 11	07:35:22	−27:42:03	242.4	−3.5	11.1 ± 0.7	3.85 ± 0.57	5.46 ± 0.56	11.54 ± 2.14
Trumpler 13	10:23:50	−60:07:41	285.5	−2.4	8.0 ± 0.6	2.30 ± 0.36	3.78 ± 0.47	9.70 ± 1.82
Pismis 12	09:20:02	−45:06:54	268.6	3.2	8.3 ± 0.5	1.15 ± 0.14	2.02 ± 0.15	5.92 ± 1.44
IC 1434	22:10:29	52:51:09	99.9	−2.7	9.0 ± 0.5	2.05 ± 0.45	3.02 ± 0.29	6.51 ± 1.34
Czernik 32	07:50:31	−29:51:12	245.9	−1.7	9.7 ± 0.5	2.02 ± 0.28	3.47 ± 0.36	10.39 ± 1.10
[FSR2007] 1325	07:50:33	−29:57:15	245.9	−1.7	10.7 ± 0.6	2.66 ± 0.40	4.32 ± 0.43	11.44 ± 1.99
Ruprecht 130	17:47:35	−30:05:12	359.2	−1.0	6.0 ± 0.6	1.04 ± 0.23	1.43 ± 0.23	3.08 ± 0.41
NGC 3519	11:04:15	−61:24:01	290.4	−1.1	7.6 ± 0.5	0.59 ± 0.15	1.03 ± 0.16	2.96 ± 0.99
King 20	23:33:17	58:28:33	112.8	−2.9	8.8 ± 0.5	2.11 ± 0.35	3.21 ± 0.33	7.30 ± 1.26
Haffner 9	07:24:43	−17:00:00	231.8	−0.6	9.9 ± 0.6	2.19 ± 0.31	3.60 ± 0.25	9.07 ± 1.54
Czernik 31	07:37:00	−20:31:05	236.2	0.2	9.9 ± 0.5	1.76 ± 0.29	2.35 ± 0.27	4.20 ± 0.67
NGC 2421	07:36:12	−20:37:48	236.3	0.1	9.6 ± 0.5	3.43 ± 0.50	4.64 ± 0.46	8.28 ± 1.43
Lynga 12	16:46:08	−50:45:04	335.7	−3.5	6.2 ± 0.6	1.03 ± 0.24	1.66 ± 0.24	4.13 ± 1.22
Ruprecht 30	07:42:32	−31:27:20	246.4	−4.0	10.1 ± 0.6	1.66 ± 0.33	2.44 ± 0.29	5.53 ± 1.11
Lynga 2	14:24:14	−61:21:30	313.8	−0.4	7.4 ± 0.5	–	–	2.92 ± 0.42[b]
Herschel 1	07:47:04	00:01:16	219.4	12.4	8.2 ± 0.5	–	–	0.86 ± 0.09[b]
				Complementary sample				
NGC 188	00:47:55	85:15:18	122.9	22.4	9.1 ± 0.5	2.54 ± 0.32	4.71 ± 0.38	15.88 ± 2.38
M 67	08:51:26	11:48:00	215.7	31.9	8.6 ± 0.5	1.63 ± 0.23	3.19 ± 0.15	13.10 ± 2.26
NGC 4337	12:24:05	−58:07:05	299.3	4.6	7.2 ± 0.5	1.62 ± 0.25	2.75 ± 0.24	7.53 ± 1.55
NGC 2439	07:40:45	−31:41:18	246.4	−4.5	9.9 ± 0.6	2.62 ± 0.40	4.39 ± 0.39	11.90 ± 1.51
Collinder 110	06:38:48	02:03:49	209.6	−1.9	9.8 ± 0.5	6.34 ± 1.20	7.08 ± 0.78	9.57 ± 1.20
Collinder 261	12:38:06	−68:22:31	301.7	−5.5	7.0 ± 0.5	3.13 ± 0.52	5.28 ± 0.48	16.10 ± 3.06
Czernik 37	17:53:17	−27:22:10	2.2	−0.6	6.6 ± 0.6	0.57 ± 0.08	1.20 ± 0.11	5.34 ± 1.64
Collinder 351	17:49:02	−28:44:27	0.6	−0.5	6.3 ± 0.6	0.59 ± 0.15	0.96 ± 0.13	2.62 ± 0.74
NGC 3680	11:25:39	−43:13:26	286.8	16.9	7.8 ± 0.5	0.45 ± 0.10	0.73 ± 0.10	2.10 ± 0.66
NGC 6216	16:49:24	−44:43:17	340.7	0.0	6.1 ± 0.7	1.82 ± 0.27	2.73 ± 0.24	6.08 ± 0.73
BH 200	16:49:55	−44:11:15	341.1	0.2	6.2 ± 0.5	1.08 ± 0.17	1.79 ± 0.22	4.82 ± 0.85

[a] The R_G values were obtained from the distances in Table 2, assuming that the Sun is located at 8.0 ± 0.5 kpc from the Galactic Centre (Reid 1993).
[b] No profile fits could be performed, and r_t was assumed to be equal to the cluster's limiting radius (Section 3.2).

number of stars within concentric annular regions and dividing this number by the ring's area.

The ring's widths were varied from 0.5 to 1.50 arcmin, in steps of 0.25 arcmin, and the set of data was superimposed on the same RDP. This strategy was adopted to improve statistics and because the narrower rings are more adequate to sample the central cluster regions, with greater stellar densities, while the larger rings are ideal to probe the external regions, where larger fluctuations induced by field stars become more severe (e.g. Maia, Corradi & Santos 2010). Uncertainties in star counts come from Poisson statistics. The background level (σ_{bg}) and its 1σ fluctuation were estimated by taking into account the average and dispersion of the stellar densities corresponding to the rings beyond the limiting radius (R_{lim}). Here, R_{lim} is the distance of the cluster centre beyond which the stellar densities fluctuate around a nearly constant value (σ_{bg}).

For each tentative centre, we fitted the corresponding background-subtracted RDP using the model of King (1962), defined by

$$\sigma(r) \propto \left[\frac{1}{\sqrt{1+(r/r_c)^2}} - \frac{1}{\sqrt{1+(r_t/r_c)^2}}\right]^2. \quad (1)$$

The fits were performed by using a grid of r_c (varying from 0.1 to 30 arcmin) and r_t (varying from 0.1 to 60 arcmin). After stepping through all coordinates in the grid, we searched for the α, δ pair that resulted in the minimum χ^2 and, at the same time, the highest density in the central cluster region. That is, we searched for central coordinates that resulted in a smooth RDP with considerable stellar overdensity compared with the background. We also performed independent fits of Plummer (1911) profiles to each cluster RDP

$$\sigma(r) \propto \left[\frac{1}{1+(r/a)^2}\right]^2, \quad (2)$$

in order to obtain estimates of its half-mass radius through the relation: $r_{hm} \sim 1.3a$.

All RDPs were normalized to unity at the innermost radial bins and we summed in quadrature the 1σ fluctuation of the background density to each background-subtracted bin. The results of our procedure are shown in Fig. 3 for six clusters. The complete set of figures for the rest of our sample is shown in the Appendix, which is available online. As can be noted from this figure, both King and Plummer profiles are nearly indistinguishable in the inner regions of each cluster, but differ in the outer parts, where the King profiles have better performance. The results for the structural parameters (already converted to pc using the distance moduli in Table 2) are listed in Table 1.

Table 2. Fundamental parameters, mean proper motion components and crossing times for the studied OCs.

Cluster	$(m-M)_0$ (mag)	d (kpc)	$E(B-V)$ (mag)	log (t yr^{-1})	[Fe/H] (dex)	$\langle\mu_\alpha\rangle$ (mas yr^{-1})	$\langle\mu_\delta\rangle$ (mas yr^{-1})	t_{cr} (Myr)
				Main sample				
Haffner 11	13.45 ± 0.40	4.90 ± 0.90	0.59 ± 0.10	8.90 ± 0.10	0.00 ± 0.17	-1.492 ± 0.183	3.170 ± 0.179	1.07 ± 0.12
Trumpler 13	13.10 ± 0.40	4.17 ± 0.77	0.63 ± 0.10	8.10 ± 0.10	-0.06 ± 0.13	-6.742 ± 0.028	4.104 ± 0.090	3.32 ± 1.26
Pismis 12	11.48 ± 0.40	1.98 ± 0.36	0.55 ± 0.05	9.20 ± 0.10	0.00 ± 0.17	-6.677 ± 0.211	4.802 ± 0.166	0.93 ± 0.11
IC 1434	12.43 ± 0.30	3.07 ± 0.42	0.49 ± 0.10	8.50 ± 0.10	-0.06 ± 0.20	-3.895 ± 0.035	-3.346 ± 0.157	1.07 ± 0.11
Czernik 32	12.50 ± 0.15	3.16 ± 0.22	0.85 ± 0.05	9.10 ± 0.10	-0.13 ± 0.23	-2.948 ± 0.141	2.488 ± 0.123	1.35 ± 0.15
[FSR2007] 1325	13.30 ± 0.40	4.57 ± 0.84	1.14 ± 0.10	7.00 ± 0.20	0.22 ± 0.17	-2.715 ± 0.071	3.436 ± 0.082	1.97 ± 0.41
Ruprecht 130	11.50 ± 0.40	2.00 ± 0.37	1.22 ± 0.10	8.40 ± 0.10	0.14 ± 0.20	0.406 ± 0.223	-1.843 ± 0.056	0.57 ± 0.10
NGC 3519	11.19 ± 0.40	1.70 ± 0.31	0.17 ± 0.10	8.70 ± 0.10	0.18 ± 0.15	-6.438 ± 0.079	3.116 ± 0.069	1.24 ± 0.27
King 20	12.11 ± 0.40	1.73 ± 0.32	0.89 ± 0.10	8.20 ± 0.20	0.28 ± 0.18	-2.667 ± 0.128	-2.630 ± 0.164	2.06 ± 0.24
Haffner 9	12.30 ± 0.30	2.64 ± 0.49	0.80 ± 0.10	8.55 ± 0.15	-0.13 ± 0.23	-0.940 ± 0.231	0.662 ± 0.441	0.87 ± 0.09
Czernik 31	11.95 ± 0.30	2.88 ± 0.40	0.60 ± 0.10	8.00 ± 0.40	0.05 ± 0.20	-1.946 ± 0.138	3.035 ± 0.130	0.98 ± 0.14
NGC 2421	11.60 ± 0.40	2.46 ± 0.34	0.55 ± 0.10	7.75 ± 0.30	-0.13 ± 0.23	-3.148 ± 0.108	3.085 ± 0.112	2.75 ± 0.29
Lynga 12	11.15 ± 0.40	2.09 ± 0.39	0.88 ± 0.15	8.70 ± 0.15	0.00 ± 0.29	-2.318 ± 1.004	-3.749 ± 0.851	0.12 ± 0.02
Ruprecht 30	12.90 ± 0.40	3.80 ± 0.70	0.63 ± 0.10	7.50 ± 0.20	0.00 ± 0.29	-2.026 ± 0.193	3.091 ± 0.264	0.62 ± 0.18
Lynga 2	9.90 ± 0.30	0.95 ± 0.13	0.40 ± 0.10	7.90 ± 0.30	-0.13 ± 0.23	-6.683 ± 0.093	-4.681 ± 0.096	–
Herschel 1	7.35 ± 0.40	0.29 ± 0.05	0.06 ± 0.15	8.65 ± 0.65	0.00 ± 0.23	0.568 ± 0.269	-4.148 ± 0.189	–
				Complementary sample				
NGC 188	11.30 ± 0.20	1.82 ± 0.17	0.13 ± 0.05	9.70 ± 0.15	0.00 ± 0.17	-2.312 ± 0.169	-0.940 ± 0.081	2.72 ± 0.23
M 67	9.45 ± 0.20	0.78 ± 0.07	0.06 ± 0.05	9.60 ± 0.10	-0.06 ± 0.13	-10.982 ± 0.154	-2.946 ± 0.187	4.78 ± 0.42
NGC 4337	11.65 ± 0.20	2.14 ± 0.20	0.49 ± 0.05	9.20 ± 0.10	-0.32 ± 0.12	-8.812 ± 0.120	1.475 ± 0.096	1.83 ± 0.17
NGC 2439	12.70 ± 0.40	3.47 ± 0.64	0.55 ± 0.10	7.25 ± 0.20	-0.22 ± 0.28	-2.275 ± 0.126	3.146 ± 0.137	1.53 ± 0.14
Collinder 110	11.57 ± 0.20	2.06 ± 0.19	0.50 ± 0.05	9.25 ± 0.10	-0.13 ± 0.23	-1.093 ± 0.145	-2.062 ± 0.155	3.87 ± 0.44
Collinder 261	12.04 ± 0.30	2.56 ± 0.35	0.33 ± 0.05	9.70 ± 0.15	0.00 ± 0.17	-6.350 ± 0.156	-2.685 ± 0.152	2.24 ± 0.21
Czernik 37	10.75 ± 0.50	1.41 ± 0.33	1.50 ± 0.10	8.70 ± 0.15	0.00 ± 0.29	0.434 ± 0.203	-0.447 ± 0.143	0.81 ± 0.09
Collinder 351	11.15 ± 0.40	1.70 ± 0.31	0.87 ± 0.15	8.85 ± 0.10	-0.06 ± 0.33	-0.237 ± 0.162	-1.700 ± 0.559	0.18 ± 0.03
NGC 3680	9.78 ± 0.40	0.90 ± 0.17	0.15 ± 0.05	9.20 ± 0.10	-0.06 ± 0.20	-7.254 ± 0.196	1.148 ± 0.231	0.69 ± 0.12
NGC 6216	11.60 ± 0.50	2.09 ± 0.48	1.04 ± 0.10	7.85 ± 0.30	0.00 ± 0.23	-1.261 ± 0.209	-2.535 ± 0.135	1.48 ± 0.14
BH 200	11.45 ± 0.20	1.95 ± 0.18	1.00 ± 0.10	7.90 ± 0.30	0.00 ± 0.23	-0.070 ± 0.176	-1.182 ± 0.127	1.19 ± 0.17

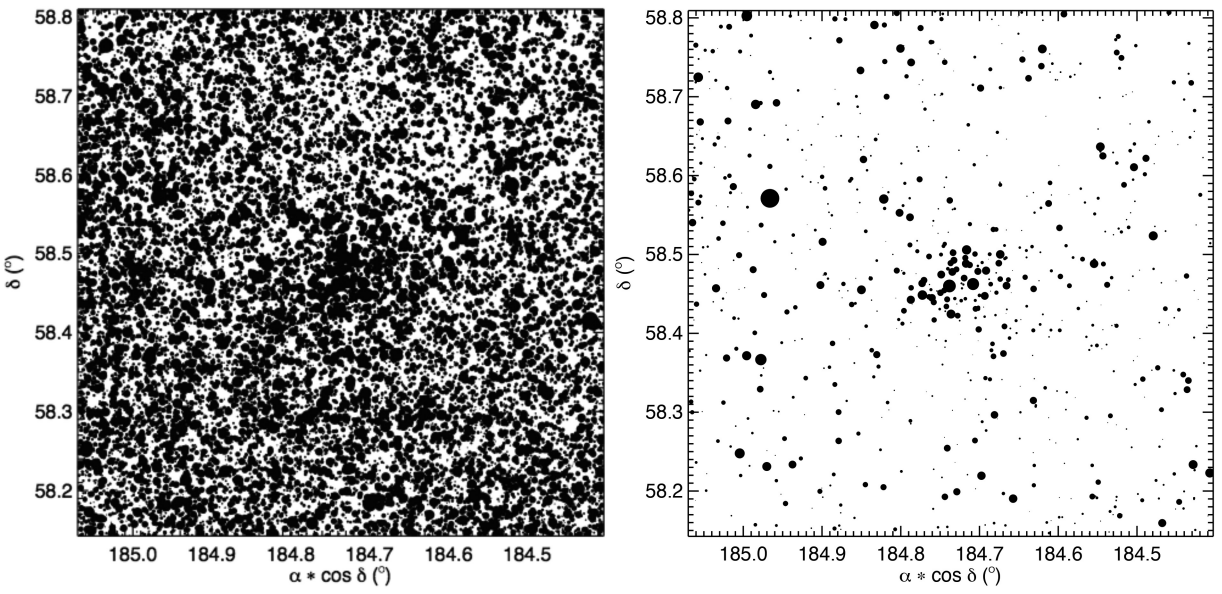

Figure 1. Left panel: skymap for stars in an area of 40 × 40 arcmin^2 centred on King 20. Only stars consistent with the filters of Arenou et al. (2018) were kept in our sample. Right panel: skymap after applying the CMD and VPD filters (see text for details).

3.3 Decontamination method

The third part of our method is devoted to the systematic search for member stars (i.e., disentanglement between cluster and field populations). To accomplish this task, we employed a decontamination algorithm, which explores the three-dimensional (3D) astrometric space ($\mu_\alpha \cos\delta$, μ_δ, ϖ) defined by stars in the cluster region and in a comparison field, and establishes membership likelihoods. Our method is fully described in Angelo et al. (2019a), for which we provide an overview in what follows.

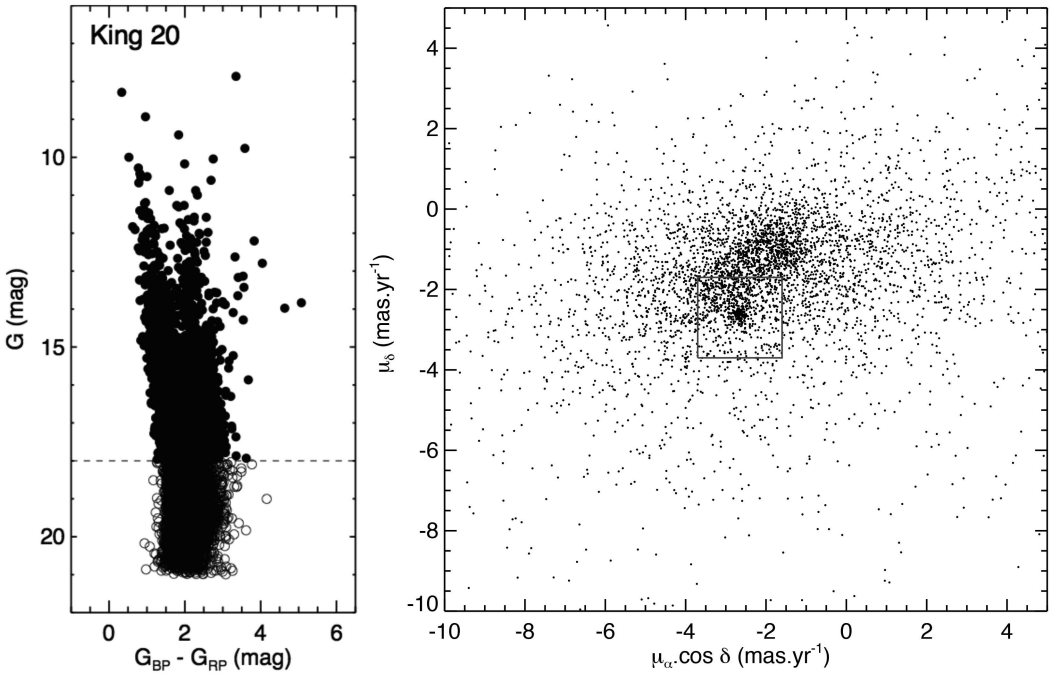

Figure 2. Left panel: CMD $G \times (G_{\rm BP} - G_{\rm RP})$ for those stars in the skymap of King 20 shown in Fig. 1. The dashed line represents the magnitude filter applied to the photometric data. Filled (open) circles represent stars brighter (fainter) than $G = 18$ mag. Right panel: VPD for stars with $G \leq 18$ mag in the region of King 20. The green square (2×2 mas yr^{-1}) shows the VPD filter (see text for details).

The main assumption of the method is that stars in a cluster must be more concentrated in a given region of the 3D space compared with field stars. This was the same principle assumed in Cantat-Gaudin et al. (2018a) and extensively employed in Cantat-Gaudin et al. (2018b). First, we took photometric and astrometric data for all stars located within the clusters' $r_{\rm t}$ (Section 3.2) and restricted this set of data to those stars inside the box defined in the clusters' VPD (see Section 3.1 and Fig. 2). From now on, the magnitude filter (as exemplified in the left panel of Fig. 2) was dismissed and our data were subject only to the filters of Arenou et al. Stars inside a concentric annular comparison field (internal radius equal to $3r_{\rm t}$) were also selected following the same filtering process. For all investigated clusters, the area of the comparison field corresponds to three times the cluster area, which allowed a proper sampling of the astrometric space without oversampling.

Then, the astrometric space defined by our data is subdivided into 3D cells (see section 3.2 of Angelo et al. 2019a) and the dispersion of data in both cluster and field samples are statistically compared. A membership likelihood (l_i) is computed for the ith star by using normalized multivariate Gaussian distributions, which take into account the three astrometric parameters simultaneously together with the associated uncertainties. The calculation also incorporates the correlations between parameters (equations 1 and 2 of Angelo et al. 2019a; see also Dias et al. 2018). The total likelihood of a group of stars is then taken multiplicatively, from which we defined an objective function analogous to the entropy of the parameter space,

$$S = -\log\left(\prod_{i=1}^{n} l_i\right), \tag{3}$$

where n is the number of stars within a given 3D cell. The same calculation was performed for both cluster and field samples.

Those cells for which $S_{\rm cluster} < S_{\rm field}$ were identified, and cluster stars within them were flagged ('1') as possible members. For cluster stars within those cells, we additionally computed an exponential factor ($L_{\rm star}$; equation 4 of Angelo et al. 2019a), which evaluates the overdensity of cluster stars within a given cell (flagged as '1') relatively to the whole grid configuration. This was a necessary procedure to ensure that only significant local overdensities, statistically distinguishable from the distribution of field stars, would receive appreciable membership likelihoods. Finally, cell sizes are increased and decreased by one-third of their original sizes in each dimension and the procedure is repeated. The final likelihood for a given star corresponds to the median of the set of $L_{\rm star}$ values taken through the whole grid configurations.

We illustrate the results of the proposed method by applying it to the well-known OC NGC 188. In the top-left panel of Fig. 4, we can see that the highest membership stars ($L_{\rm star} \gtrsim 0.7$) define clear evolutionary sequences in the $G \times (G_{\rm BP} - G_{\rm RP})$ CMD and also detached concentrations in both VPD (top-right panel) and $\varpi \times G$ magnitude plots (bottom panel). Symbol colours were given according to the membership likelihoods, as indicated in the colour bars. Large filled circles represent member stars and small black dots are stars in a comparison field. The solid line in the decontaminated CMD represents a best-fitting $\log(t\ {\rm yr}^{-1}) = 9.7$ solar metallicity PARSEC isochrone (Bressan et al. 2012; see Section 4). The dashed line is the same isochrone displaced vertically by -0.75 mag and represents the locus of unresolved binary stars with equal-mass components. The fundamental astrophysical parameters are indicated.

4 RESULTS

The procedures outlined in Section 3 were applied to our complete sample (Tables 1 and 2). The results are shown in the decontaminated CMDs of Fig. 5 for six of our investigated OCs. CMDs for the remaining clusters are shown in the Online Appendix. We considered only stars with membership likelihoods $L \geq 0.7$, as

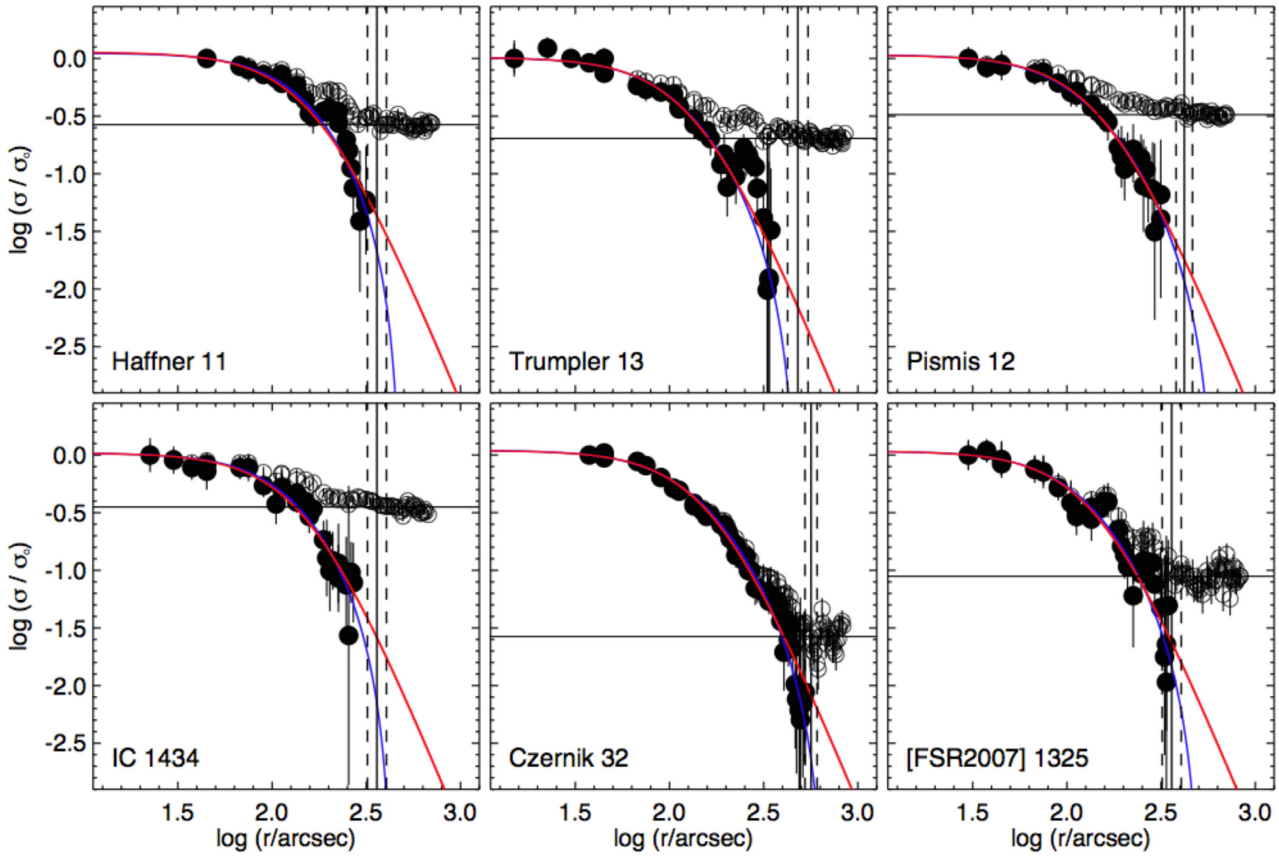

Figure 3. Background-subtracted and normalized RDPs (filled symbols) for six of the investigated OCs (RDPs for other clusters are shown in the Online Appendix). The non-subtracted RDPs are plotted with open circles. The blue (red) solid lines represent the best-fitting King (Plummer) profile to our data and the horizontal solid line represents the mean background density ($\sigma_{\rm bg}$). The vertical solid and dashed lines represent, respectively, the cluster's limiting radius ($R_{\rm lim}$) and its uncertainty.

these objects define key evolutionary regions such as the lower main sequence, the turn-off and the red clump, which allowed the estimation of fundamental astrophysical parameters via isochrone fitting, as explained below. All CMDs have been plotted with the same ranges in magnitude and colour indices to allow a prompt comparison between clusters in terms of magnitude interval, extension of the main sequence and interstellar reddening.

In some cases (e.g. Haffner 9 and Lynga 12), colour filters (analogous to those employed by Bica & Bonatto 2011) were applied to remove very reddened stars before the run of the decontamination method. Those stars are more probably part of the disc population. Proper motions of these clusters are comparable with the bulk movement of the field (Fig. A7), which diminishes the contrast between both populations in the astrometric space, increasing the presence of outliers in the final solution. It was useful to apply colour filters in order to reduce the residual contamination, thus resulting in clearer evolutionary sequences in the corresponding CMDs.

4.1 Isochrone fitting

The fundamental astrophysical parameters, age, distance modulus, reddening and metallicity, that is, $\log t$, $(m - M)_0$, $E(B - V)$ and [Fe/H], respectively, were derived using the automated isochrone fitting module of the ASteCA[2] (Automated Stellar Cluster Analysis) code. The method is fully presented and tested in section 2.9 of Perren, Vázquez & Piatti (2015). Briefly, it consists of the generation of synthetic clusters from theoretical isochrones with a variety of parameters and the selection of the best fit through a genetic algorithm.

Before the run of the automated method, we performed visual isochrone fits in order to obtain reasonable initial guesses, $\log t_{\rm ini}$, $(m - M)_{0,\,\rm ini}$, $E(B - V)_{\rm ini}$ and $[{\rm Fe/H}]_{\rm ini}$, for the fundamental parameters. For each cluster, the initial guess for the distance modulus was based on the mean parallax, $\langle\varpi\rangle$, of high membership stars ($L \geq 0.7$; Fig. 5) through the relation $(m - M)_0 = 5 \log (100/\langle\varpi\rangle)$, with $\langle\varpi\rangle$ expressed in mas, as usual. $E(B - V)_{\rm ini}$ was taken from the DAML02 catalogue. When necessary, some adjustments were applied to both parameters in order to obtain a reasonable fit to the locus of points along the main sequence. At this stage, solar metallicity isochrones were employed. After that, $\log t_{\rm ini}$ and $[{\rm Fe/H}]_{\rm ini}$ were estimated from brighter stars along the more evolved sequences. The relative distance between the cluster turn-off and the red clump (if present) is a very useful constraint for isochrone fitting.

Taking the initial guesses for the fundamental parameters, we then restricted the parameter space covered by the PARSEC models and, as input to the ASteCA code, the intervals were sampled according to the following specifications:

(i) $(m - M)_{0,\,\rm ini} - 0.5 \leq (m - M)_0 \leq (m - M)_{0,\rm ini} + 0.5$, in steps of $\Delta(m - M)_0 = 0.1$ mag;

[2]Available at https://asteca.github.io/.

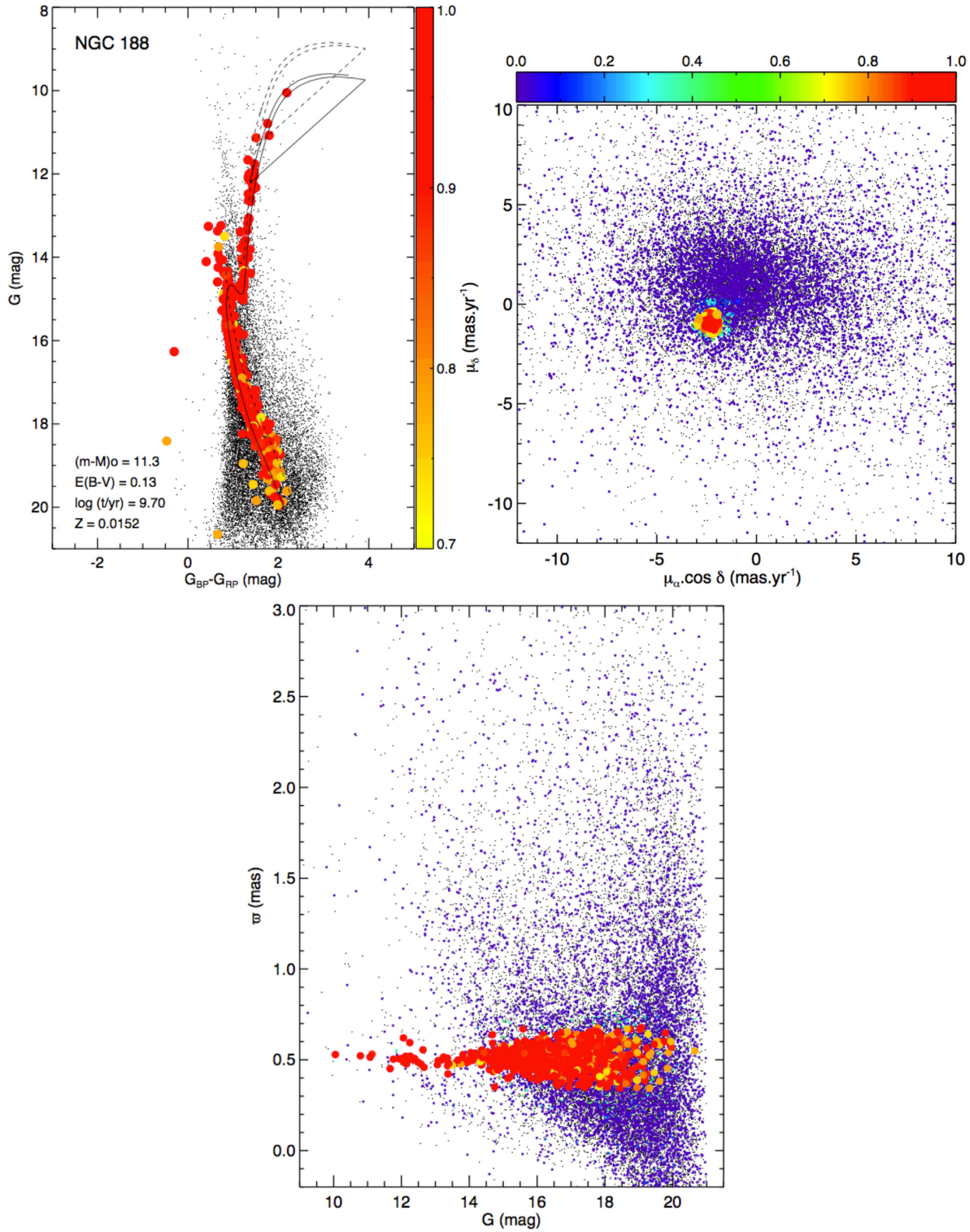

Figure 4. Top-left panel: decontaminated CMD for NGC 188. The solid line is a solar metallicity PARSEC isochrone and the dashed line is the locus of unresolved binaries with same mass components. Top-right panel: cluster's VPD. Bottom panel: parallax versus *G* magnitude plot. In all plots, coloured symbols are stars inside the cluster's r_t and colours are attributed according to the membership likelihoods. Large filled circles represent member stars and small black dots represent stars in a comparison field.

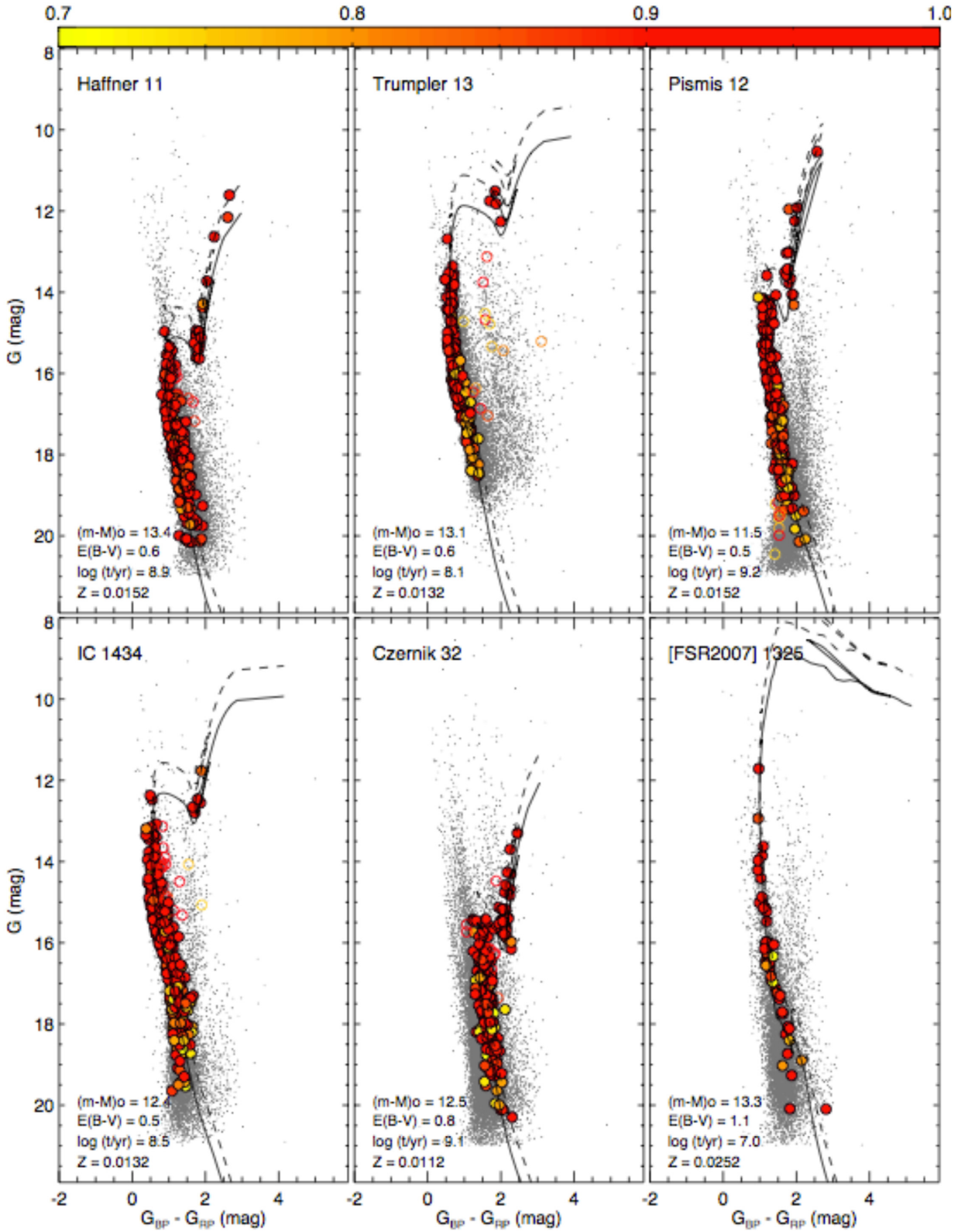

Figure 5. CMDs $G \times (G_{BP} - G_{RP})$ for the OCs Haffner 11, Trumpler 13, Pismis 12, IC 1434, Czernik 32 and [FSR2007] 1325. The symbol convention is the same as adopted in Fig. 4. Only stars with $L \geq 0.7$ are shown. Member stars are plotted as filled circles. Best-fitting PARSEC isochrones (solid lines) and equal-mass binary locii (dashed lines) are also indicated.

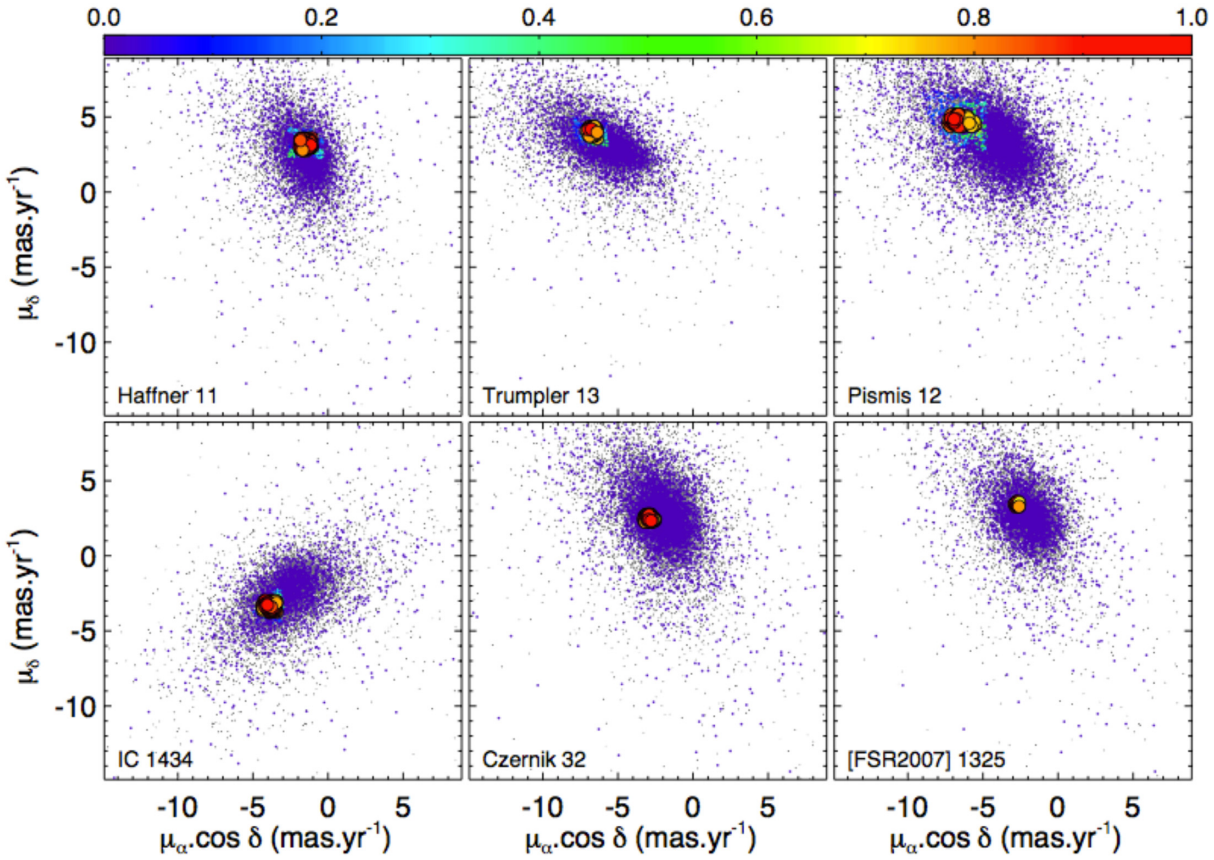

Figure 6. VPDs for six of our studied OCs. The symbol convention is the same as adopted in Fig. 4.

(ii) $E(B-V)_{\rm ini} - 0.5 \leq E(B-V) \leq E(B-V)_{\rm ini} + 0.5$, in steps of $\Delta E(B-V) = 0.02$ mag;
(iii) $Z_{\rm ini} - 0.01 \leq Z \leq Z_{\rm ini} + 0.01$, in steps of $\Delta Z = 0.002$.

Here, the overall metallicity Z can be associated with the iron abundance ratio [Fe/H] according to the approximate relation [Fe/H] $\sim \log(Z/Z_{\odot})$ (Bonfanti, Ortolani & Nascimbeni 2016), with $Z_{\odot} = 0.0152$ (Bressan et al. 2012). Besides the intervals specified above, ASteCA builds synthetic clusters with total masses M between 10 and 10 000 $M_{\odot}$ (steps of $\Delta M = 100\,M_{\odot}$) and containing fractions of binary stars ($f_{\rm bin}$) varying from 0 to 1 (steps of $\Delta f_{\rm bin} = 0.2$), with the mass ratio between the primary and secondary stars fixed in a pre-defined value of 0.7. No magnitude cuts have been applied during the isochrone fitting process. With the above intervals, $\sim 10^6$ models were compared with the observed CMD for each studied OC. The CMDs in Fig. 5, besides those in the Online Appendix, show that the method provided adequate fits, with the corresponding isochrones properly describing the evolutionary sequences defined by the more probable member stars.

Figs 6 and 7 exhibit, respectively, the cluster VPDs and the $\varpi \times G$ magnitude plots after applying our decontamination method. The same symbols convention of Fig. 4 were employed here. The corresponding figures for the rest of our sample are shown in the Online Appendix.

4.2 Comparison with previous works

Cantat-Gaudin et al. (2018b) performed a uniform characterization of 1212 Galactic clusters by applying an unsupervised membership assignment code to the *Gaia* DR2 data contained within the fields of those clusters. Their decontamination method is based on the same strategy as the present work, which is to look for concentrations of cluster stars in the astrometric space that are more tightly distributed than field stars. A basic difference is that the method of Cantat-Gaudin et al. (2018a) performs comparisons between the distribution of astrometric data for cluster stars with that for randomly generated samples. In our case, we have employed *observed* samples of stars in comparison fields (Section 3.3). Besides, the sampling of the astrometric space in Cantat-Gaudin et al. (2018a) is based on the k-means clustering algorithm incorporated in the membership assignment method UPMASK (Krone-Martins & Moitinho 2014). In our case, the astrometric space is sampled using a uniform grid of cells with varying sizes (Section 3.3).

We performed a direct comparison between the mean astrometric parameters ($\langle \mu_{\alpha} \cos\delta \rangle$, $\langle \mu_{\delta} \rangle$, $\langle \varpi \rangle$) derived for OCs in the present paper and the corresponding ones obtained by Cantat-Gaudin et al. (2018b). Fig. 8 compares the results for 22 OCs in common with both studies (data for Collinder 351, [FSR2007] 1325, Herschel 1, Lynga 12 and Ruprecht 30 are absent in Cantat-Gaudin et al. 2018b). We can see that, despite their differences, both methods recovered almost the same mean parameters. In our case, the error bars in Fig. 8 correspond to the intrinsic dispersion of the astrometric parameters considering each sample of member stars (Sections 3 and 4). Concerning the parallaxes, to the final dispersions we have added in quadrature a systematic uncertainty of 0.1 mas affecting the astrometric solution in *Gaia* DR2 (Luri et al. 2018).

Fourteen OCs in our main sample (Tables 1 and 2) were also investigated by Bica & Bonatto (2005, 2011) and Bica et al. (2006).

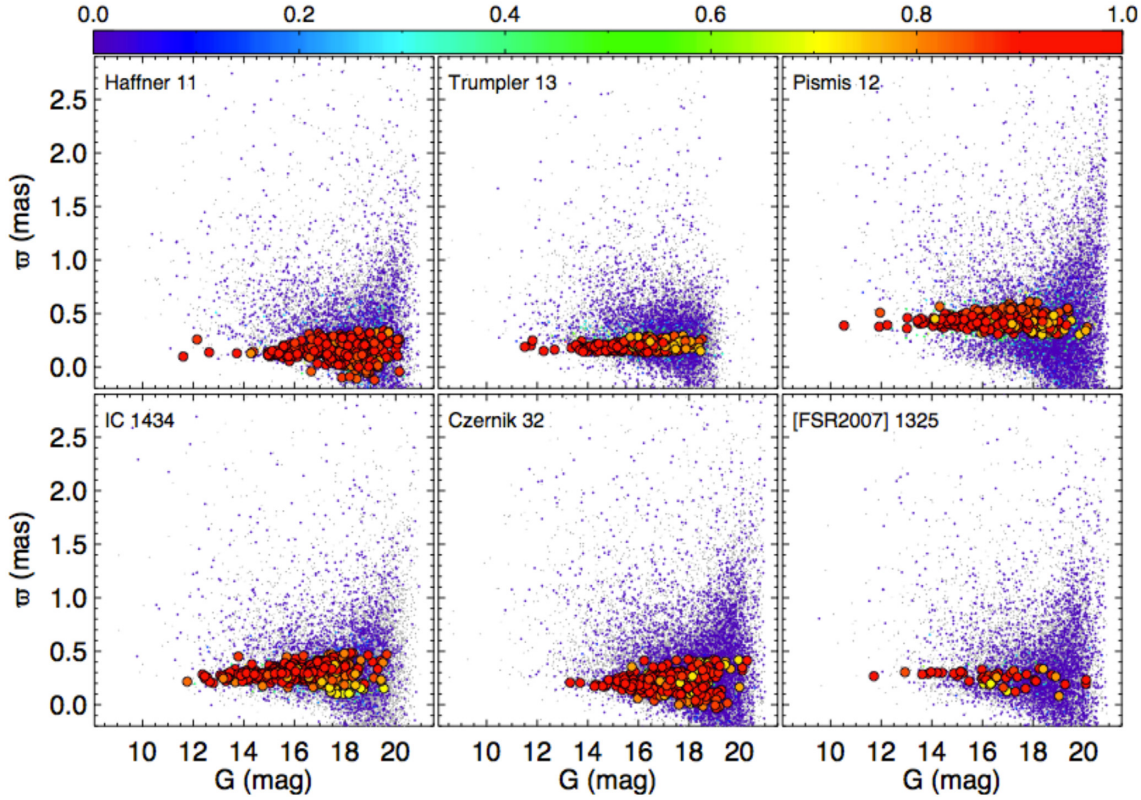

Figure 7. $\varpi \times G$ magnitude for six of our investigated OCs. Symbol convention is the same as employed in Fig. 4.

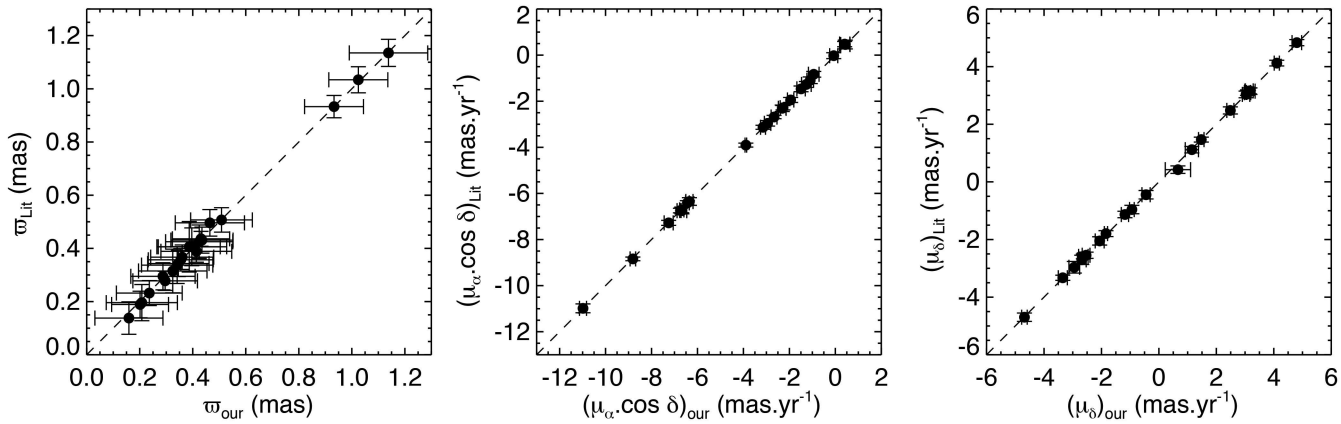

Figure 8. Comparison between mean cluster parameters derived in the present study ($\langle\mu_\alpha \cos\delta\rangle_{\rm our}$, $\langle\mu_\delta\rangle_{\rm our}$, $\langle\varpi\rangle_{\rm our}$) and those obtained by Cantat-Gaudin et al. (2018b) ($\langle\mu_\alpha \cos\delta\rangle_{\rm lit}$, $\langle\mu_\delta\rangle_{\rm lit}$, $\langle\varpi\rangle_{\rm lit}$). In our sample, error bars correspond to the intrinsic dispersion (σ_{μ_α}, σ_{μ_δ}, σ_ϖ) obtained from each sample of cluster members (for σ_ϖ, we have added in quadrature a systematic uncertainty of 0.1 mas). The dashed line is the identity relation.

The OCs NGC 2421 and [FSR2007] 1325 were included as they are projected in the same regions of Czernik 31 and Czernik 32, respectively (see Section 4.3). Fig. 9 shows comparisons between the fundamental parameters $E(B-V)$, $(m-M)_0$ and $\log(t)$ derived in the present study and those in the literature. As we can see, there is not a tight agreement between both sets of parameters and some severe discrepancies are present. The main reason for such discrepancies, besides the use of different sets of isochrones and CMD fitting techniques, may be related to the CMD decontamination procedures and selection of member stars. The procedures employed in the series of papers of Bica & Bonatto are based on the use of JHK_s photometry from the 2MASS catalogue and on the analysis of $J \times (J-H)$ and $J \times (J-K_s)$ CMDs built for stars in the cluster regions and for comparison fields.

Briefly, their method consists of a decontamination algorithm (Bonatto & Bica 2007), which builds 3D CMDs, with J, $(J-H)$ and $(J-K_s)$ axes, divided into cells with different grid configurations, and assigns memberhip probabilities according to the local over-density of stars in the cluster CMD compared with the distribution of field stars in the same data domain in the field CMD. Keeping those stars with higher memberships allowed the construction of decontaminated CMDs. Residual contamination, especially in the case of very reddened clusters projected close to the Galactic plane, is eliminated with the use of colour filters (see figs 1–3 of Bica &

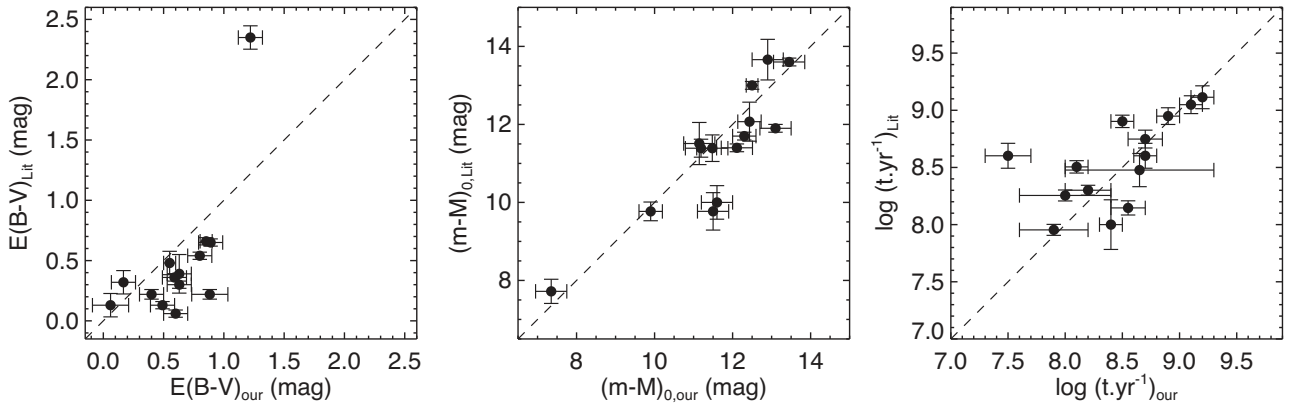

Figure 9. Comparison between the fundamental parameters $E(B-V)$, $(m-M)_0$ and $\log t$ derived in the present study and those obtained in the literature. The dashed line is the identity relation.

Bonatto 2011). Then, visual isochrone fits were performed and the fundamental astrophysical parameters were derived.

Our method has the advantage of relying not only on photometric data but also on high-precision astrometric information. In particular, in the case of low-contrast OCs, we advocate that different types of data should be combined in a joint analysis for a more rigorous selection of member stars. In general, our CMDs are typically ∼1–5 mag deeper than those built with 2MASS filters, which allows better constraints for isochrone fitting. Besides, the parameters obtained by Bica & Bonatto assumed fixed solar values for the cluster metallicities, for simplicity.

4.3 Comments on individual clusters

In this section, we highlight some comments about two binary cluster candidates, Czernik 31−NGC 2421 and Czernik 32−[FSR2007] 1325, and also for three other OCs, Ruprecht 30, Ruprecht 130 and NGC 3519, which were classified as asterisms or had their real physical nature inconclusively determined in previous studies.

4.3.1 Czernik 31 and NGC 2421

The pair Czernik 31−NGC 2421 is present in the list of candidate binary clusters of de La Fuente Marcos & de La Fuente Marcos (2009). Fig. 10 shows both clusters with member stars highlighted. Not only are they projected in the same region, but they seem to form a physical pair, as their distance moduli, ages and colour excesses are compatible with each other within uncertainties (Table 2). Besides, the position of the centroids in their corresponding VPDs are quite similar (Fig. A7).

NGC 2421 presents a fluctuation in its RDP between $6.5 \lesssim r \lesssim 8.5$ arcmin ($2.6 \lesssim \log(r\,\mathrm{arcsec}^{-1}) \lesssim 2.7$ in Fig. A1), where members stars with $12.5 \leq G \leq 19.8$ mag (stellar masses in the range $0.70 \lesssim M \lesssim 4.9$ $M_\odot$) are found. Less noticeably, Czernik 31 presents a fluctuation in stellar density in the external region $3.5 \lesssim r \lesssim 4.5$ arcmin ($2.3 \lesssim \log(r\,\mathrm{arcsec}^{-1}) \lesssim 2.4$ in Fig. A1), where we find member stars with G magnitudes in the range $15.3 \leq G \leq 19.8$ mag (which converts to stellar masses in the range $0.85 \lesssim M \lesssim 2.2$ $M_\odot$, considering the cluster distance modulus, metallicity and age; see Section 4 and Table 2). Both density fluctuations define these clusters' corona, and these external structures may be the result of tidal interactions between them. The overlap of their tidal radii, as seen in Fig. 10, reinforces the hypothesis of close gravitational

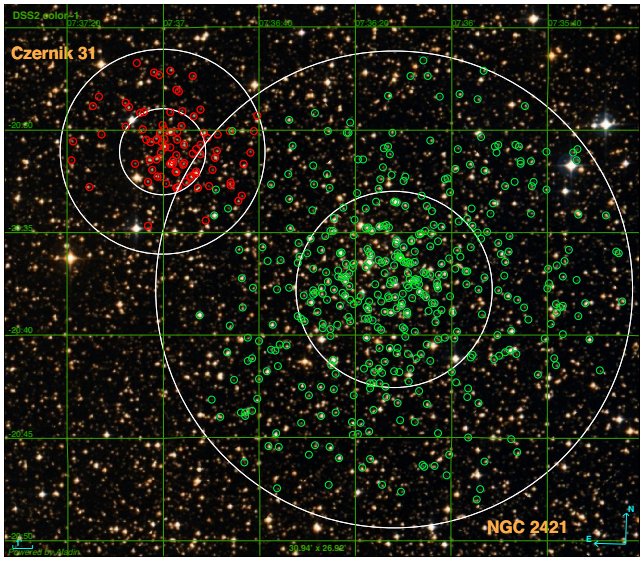

Figure 10. DSS image (31×27 arcmin^2) of the pair Czernik 31−NGC 2421. Member stars of each cluster are identified with coloured circles. Concentric white circles represent r_c and r_t radii for each cluster. North is up and east is to the left.

interaction. Following Innanen et al. (1972), for two clusters separated by a distance smaller than three times the outer radius of each cluster, the amount of mutual disruption is not negligible. In fact, the dynamics of interaction between Czernik 31 and NGC 2421 could be investigated in more detail with the determination of radial velocities, in order to obtain 3D velocity vectors.

4.3.2 Czernik 32 and [FSR2007] 1325

The OC [FSR2007] 1325 is listed in the survey of Froebrich, Scholz & Raftery (2007), who used star density maps constructed from the 2MASS catalogue to locate a sample of star clusters at Galactic latitudes $|b| < 20°$. It is projected southwards of Czernik 32, as shown in Fig. 11.

The results in Table 2 show that these two clusters present distances that are incompatible with the hypothesis of a pair of interacting OCs. The corresponding colour excesses are also different. Besides, their RDPs (Fig. 3) are well fitted by the King profile until $r \sim r_t$, and do not exhibit any noticeable distorsions that

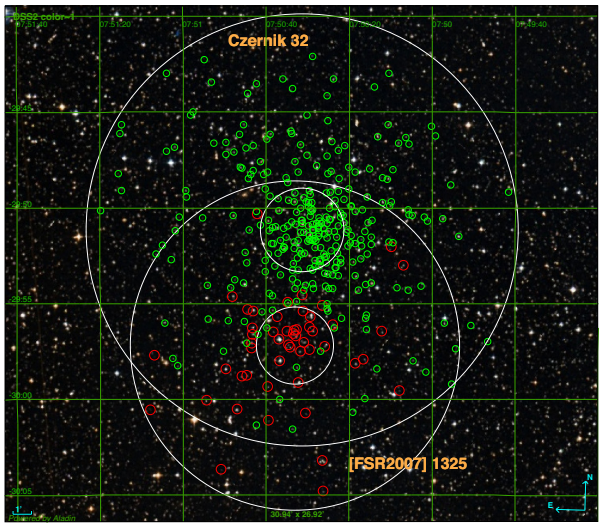

Figure 11. Same as Fig. 10, but showing the pair Czernik 32−[FSR2007] 1325. Image size is 31 × 27 arcmin^2.

could be the result of tidal interactions. Therefore, we advocate that the apparent proximity of Czernik 32 and [FSR2007] 1325 along the line of sight may be a projection effect.

4.3.3 *Ruprecht 30 and Ruprecht 130*

Carraro et al. (2010) performed star counts in the direction of Ruprecht 30 using deep photometry in the V filter (down to $V \sim 20$ mag) and did not verify any obvious overdensities (their fig. 4), thus suggesting that there is no cluster at the location of Ruprecht 30. In fact, establishing its physical nature is not a trivial task, as it is not a heavily populated stellar concentration and it is projected against a dense background. During the pre-analysis procedure (Section 3.1), we could only find some clues about its physical existence after applying magnitude filters, like that illustrated in Fig. 2. Star counts on unfiltered data can mask the physical existence of this cluster, because of the prevalence of the field population. After running our decontamination method, we concluded that it is a genuine stellar aggregate, which was the same conclusion as Bica & Bonatto (2011).

Ruprecht 130 was included in the list of 'borderline cases' as stated by Bica & Bonatto (2011), because no definitive conclusions could be drawn regarding its physical nature based on the decontaminated $J \times (J - K_s)$ CMD (their fig. 3). They suggest the presence of a real cluster, which is confirmed by our analysis. Ruprecht 130 VPD (Fig. A7) exhibits a real concentration of stars and its CMD (Fig. A3) reveals unambiguous evolutionary sequences.

4.3.4 *NGC 3519*

This OC is also called Ruprecht 93 and it was analysed by Cheon, Sung & Bessell (2010) using *UBVI* CCD photometry. They were unable to confirm the existence of a real cluster from the spatial distribution of blue stars. They considered the absence of stars with $(U - B)_0 < 0.0$ (spectral types earlier than B9 V; see their figs 1 and 2) in the central regions of NGC 3519 as an indication that we are not facing a real OC. Here we propose a different interpretation.

The bluer stars in the CMD of NGC 3519 ($11.5 \lesssim G \lesssim 12.5$ mag, $G_{BP} - G_{RP} < 0.5$ mag; see Fig. A3) present effective temperatures and masses around ~ 8500 K and ~ 2.5 M$_\odot$, respectively,

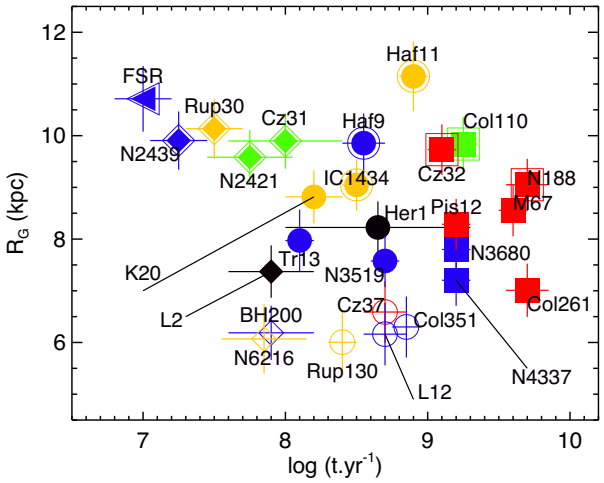

Figure 12. Galactocentric distances (R_G) and ages for the investigated OCs. Symbols are given according to Table 3 and acronyms for these clusters are shown. Lynga 2 (L2) and Herschel 1 (Her1), for which no r_c and r_{hm} could be derived (Table 1), are plotted with black symbols.

as inferred from the PARSEC models. These parameters are more compatible with spectral type A. Consequently, no B stars are expected, considering this cluster's age. Interestingly, in fig. 2 of Cheon et al. (2010) we can note that the zero-age main-sequence relation reddened by $E(B - V) = 0.25$ (which is reasonably close to our value) fits adequately a considerable number of stars with spectral types between A0 and A7, compatible with NGC 3519's turn-off (Fig. A3). Despite this, Cheon et al. arbitrarily dismissed such stars as possible members.

Consistent with the main conclusion of Bica & Bonatto (2011), here we advocate that NGC 3519 is a genuine OC, judging by the dispersion of data in its VPD and the evolutive sequences defined on its decontaminated CMD.

5 DISCUSSION

OCs have their stellar content gradually depleted as they evolve dynamically. Internal relaxation transfers energy from the (dynamically) warmer central core to the cooler outer regions (Portegies Zwart, McMillan & Gieles 2010), which causes low-mass stars to be preferentially evaporated, thus becoming part of the general field population. Stars can also be ejected from the cluster after few encounters with hard binaries (e.g. Heggie 1975; Hills 1975; Hut & Bahcall 1983). External interactions can additionally cause the gradual dispersion of an OC stellar content, such as disc shocking (Spitzer 1958; Theuns 1991) and collisions with giant molecular clouds (e.g. Ostriker, Spitzer Lyman & Chevalier 1972). It is expected that the interplay between these destructive effects causes structural changes that can be probed from the relationships between r_c, r_{hm} and r_t (Piatti et al. 2017, and references therein).

In what follows, we show relations between structural and time-related parameters. We also present some general aspects of the investigated OCs.

5.1 General characteristics of the investigated sample

Fig. 12 exhibits the Galactocentric distances as a function of age for our sample, together with cluster acronyms. Symbols were assigned according to the following convention (see Table 3): open symbols

Table 3. Symbol convention and colours used in Figs 12–15.

Age range $\log(t\ \mathrm{yr}^{-1})$	$R_G \leq 7$kpc	$7 < R_G \leq 9$kpc	$R_G > 9$ kpc
≤ 7	◁	◀	◀
(7 , 8]	◊	◆	◆
(8 , 9]	○	●	●
>9	□	■	■
Colour		c (see Fig. 14, panel a)	
Red		$c \gtrsim 0.70$	
Blue		$0.60 \lesssim c \lesssim 0.70$	
Orange		$0.40 \lesssim c \lesssim 0.60$	
Green		$c \lesssim 0.40$	

for clusters with $R_G \leq 7$ kpc, filled symbols for those with $7 < R_G \leq 9$ kpc and contoured symbols for $R_G > 9$ kpc. As explained in Table 3, our OCs were also categorized according to the age range (different symbols) and concentration parameter ($c = \log(r_t/r_c)$; different colours).

Fig. 13(a) shows that most of the investigated OCs are located between or close to the Sagittarius and Perseus arms. Their R_G vary from ∼6 to 11 kpc (Table 1). The position of the Sun and the solar circle (dashed line) are represented. Figs 13(a) and (b) show the spatial distribution of our sample along the Galactic plane and perpendicular to the disc. Almost all investigated OCs are located within ∼ 300 pc from the Galactic plane, which places them in the thin disc according to Chen et al. (2001), who derived a scaleheight of $z_h \sim 330$ pc for this Milky Way component; see also figs 2 and 11 of Brown et al. (2018). Exceptions are M 67 ($|Z| \sim 400$ pc) and NGC 188 ($|Z| \sim 700$ pc). Figs 13(c) and (d) show how ages and metallicities distribute spatially. For comparison purposes, we also plotted clusters with available distances and ages from the DAML02 catalogue (small grey dots).

The investigated clusters follow the general dispersion of data from the literature, with older clusters tending to be farther from the Galactic plane. [Fe/H] values vary from ∼−0.3 to ∼ +0.3 dex, with most of the OCs in our sample presenting solar or close to solar metallic content. Again, they are consistent with the general dispersion of data in the [Fe/H] × R_G plot, as shown in panel (d). Considering uncertainties, most of them are located within the limits of the metallicity radial gradient ($\mathrm{d[Fe/H]}/\mathrm{d}R_G = -0.086 \pm 0.009$ dex kpc^{-1}) as fitted by Netopil et al. (2016); see solid and dashed lines in panel (d).

5.2 Structural and time-related parameters

Fig. 14(a) shows the concentration parameter as a function of age for our OC sample and those in the literature (grey dots); these are taken from Kharchenko et al. 2013, as DAML02 does not provide r_t and r_c values. The concentration parameter gives some evidence regarding the OC dynamical state, as internal relaxation causes higher-mass stars to sink towards the cluster's centre and low-mass stars, preferentially, to evaporate. This leads to a successively greater core–halo differentiation (e.g. de La Fuente Marcos 1997; Portegies Zwart et al. 2001) and larger c values. Compared with OCs in the literature, most of the OCs studied here are among those with smaller c values for their ages.

The increasing degree of central concentration can be verified in Fig. 14(b), where r_c is plotted as a function of the dynamical ratio $\tau_{dyn} = \mathrm{age}/t_{cr}$. The crossing time t_{cr} (see Table 2) is a dynamical time-scale required for a typical star to cross the system. In this sense, the greater the τ_{dyn}, the more dynamically evolved an OC. t_{cr} can be defined as $t_{cr} = r_{hm}/\sigma_V$, where σ_V is the intrinsic 3D velocity dispersion of the stars. The σ_V values, converted to km s^{-1} using the distances determined in Section 4.1, were obtained from the dispersion in proper motions of member stars (Table 2), assuming that the velocity components relative to each cluster centre are isotropically distributed. With this approximation, $\sigma_V = \sqrt{3/2}\,\sigma_\mu$, where σ_μ is the dispersion of the projected angular velocities (μ), that is, $\mu = \sqrt{\mu_\alpha^2 \cos^2\delta + \mu_\delta^2}$. The uncertainties in the proper motion components were properly taken into account in the calculation of σ_μ by means of the procedure described in section 4 of van Altena (2013) and also in Sagar & Bhatt (1989).

In Fig. 14(b), we can note a general decrease in r_c as a function of τ_{dyn}, that is, clusters that have lived for many crossing times tend to present more compact central structures. Interestingly, the correlation between r_c and τ_{dyn} seems to follow two different evolutionary paths in this plot, as suggested by the dashed lines (which were plotted here just to guide the eye). Particularly, for both trends suggested in Fig. 14(b) we can see a more distinct separation between clusters with $c \gtrsim 0.70$ (red symbols) and those with $c \lesssim 0.60$ (orange and green symbols): the more concentrated ones tend to present larger τ_{dyn}. It is also noticeable from this panel that all clusters with $\log(\tau_{dyn}) > 2.2$ are older than $\log(t\ \mathrm{yr}^{-1}) > 8.3$.

The distribution of clusters with intermediate c values (blue symbols) suggests that the dynamical evolution of OCs is dominated by the internal two-body relaxation and regulated by the Galactic tidal field. In this context, the initial conditions at formation also play a role. Lynga 12 and Collinder 351 are part of the group of studied OCs with smaller Galactocentric distances and thus subject to a stronger Galactic gravitational pull, which may have accelerated their dynamical evolution. Both present $\log(\tau_{dyn}) > 3.6$ and may have suffered more severe mass loss. In turn, the old, $\log(t\ \mathrm{yr}^{-1}) > 9$, clusters NGC 4337 and NGC 3680 present c values compatible with those OCs with the highest concentrations (red symbols) and they are also among the group of more dynamically evolved ones, $\log(\tau_{dyn}) \gtrsim 3$. It is enlightening to verify that both present the same age and are placed at compatible R_G, but NGC 3680 seems more evolved, presenting the smallest r_c value in our sample. Consequently, differences in their present evolutionary stages may be linked to their properties at formation, like dissimilar original masses.

However, although [FSR2007] 1325 and NGC 2439 are young objects, $\log(t\ \mathrm{yr}^{-1}) < 7.3$, their ages surpass the corresponding crossing times, so they present some degree of dynamical evolution. Besides their ages, Galactocentric distances and τ_{dyn} are similar within uncertainties, which makes them dynamically similar to each other. Consequently, they may possibly follow close evolutionary paths as they orbit the Galaxy. Other clusters plotted with blue symbols (i.e. BH 200, Haffner 9, NGC 3519 and Trumpler 13) are in intermediate evolutionary stages. We also highlight the case of Collinder 110, which is the less concentrated OC in our sample ($c = 0.18$). Apparently, its relatively large Galactocentric distance ($R_G \sim 10$ kpc) allowed this OC to distribute its stellar content inside a less relaxed internal structure without being tidally disrupted, but on its way to dissolution.

Because the clusters are not seggregated by age along the suggested sequences in Fig. 14(b) and not distributed according to their Galactocentric distances, we speculate that both paths may be a consequence of different initial formation conditions. Indeed, a spread of r_c for clusters a few Gyr old in the Magellanic Clouds has been interpreted as the effect of black holes retained by the core as

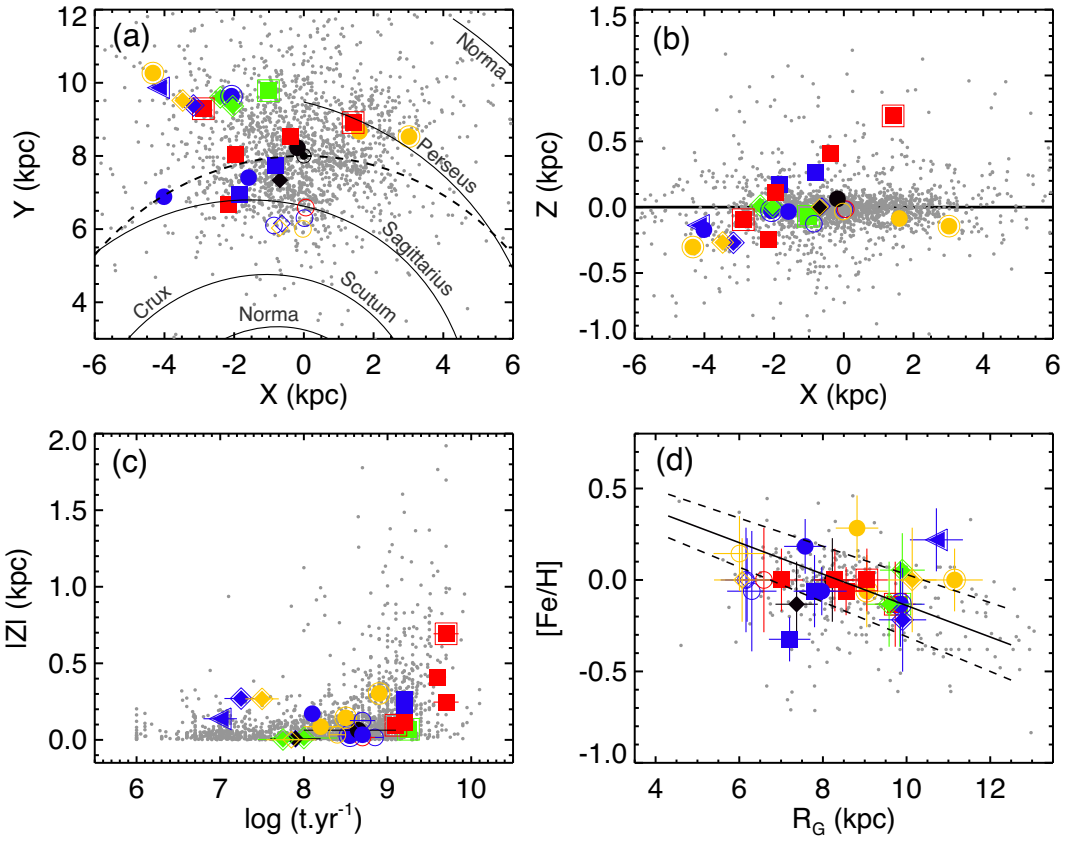

Figure 13. Distribution of the investigated OCs along the Galactic plane (panel a) and perpendicular to the disc (panel b). The positions of the spiral arms were taken from Vallée (2008). Panel (c) shows the Galactic Z coordinate as a function of cluster age and panel (d) shows the dispersion of [Fe/H] as a function of R_G. For reference, the solid line is the metallicity gradient fitted by Netopil et al. (2016); the uncertainties in this relation are represented as dashed lines. In all panels, small grey symbols represent OCs taken from the DAML02 catalogue.

the cluster evolves (Mackey et al. 2008) or, alternatively, as the result of a combination of different structure and physical properties at the moment of cluster birth and distinct stages of internal dynamical evolution (Ferraro et al. 2019). In general, clusters with larger cores are dynamically less evolved than those with smaller cores. Analogous statements can be drawn for the half-mass radii, as r_c and r_{hm} are correlated, as shown in Fig. 14(c).

The level of internal relaxation can also be inferred from the r_c/r_{hm} ratio. In fact, those with smaller r_c/r_{hm} ratios present larger c values. Following Fig. 14(b) and the discussions above, those more centrally concentrated (i.e. smaller r_c/r_{hm}) tend to be in more advanced evolutionary stages. In turn, the r_{hm}/r_t ratio can be used as a probe of the tidal influence of the Galaxy on the cluster's dynamical evolution (Baumgardt et al. 2010). Clusters for which their half-mass content fills a larger fraction of the tidal volume are subject to a larger mass loss due to tidal effects. Fig. 14(d) shows that r_c/r_{hm} and r_{hm}/r_t ratios present a positive correlation; that is, those more compact are in fact less subject to disruption by the Galactic tidal field. It is noticeable that the data along the suggested trend are not seggregated according to OC ages or Galactocentric distances.

The set of results presented in Fig. 14 suggests an overall disruption scenario in which OCs tend to become more compact structures as they evolve dynamically. This means that, in the far future, initially massive OCs will leave behind only a compact core, with most of their low-mass stellar content dispersed in the general Galactic field (de La Fuente Marcos 1996; Bonatto, Bica & Pavani 2004).

5.3 Differential tidal effects on OCs' structure

Fig. 15(a) allows us to evaluate if the r_{hm}/r_t ratio is differentially affected by the Galactic tidal field. The positions of the black open stars in the plot and their error bars represent, respectively, the mean and standard deviation of the r_{hm}/r_t ratio for OCs in three R_G bins: $R_G \leq 7$, $7 < R_G \leq 9$ and $R_G > 9$ kpc. There is no clear trend with R_G, but the dispersion in r_{hm}/r_t for OCs in the range $R_G > 9$kpc is at least 50 per cent larger compared with the other R_G bins. The smaller dispersion in r_{hm}/r_t for smaller R_G may be because these OCs are subject to a stronger Galactic tidal field. In these cases, smaller r_{hm}/r_t values favour their survival against tidal disruption.

Changes in the Galactic gravitational potential may have imprinted differential tidal effects in the OCs' outermost structures. Fig. 15(b) shows, on average, an increase in r_t as a function of the Galactocentric distance, considering the same three R_G bins of Fig. 15(a). The dispersions in r_t are also considerably larger for those located at $R_G \gtrsim 7$ kpc compared with those closer to the Galactic Centre (open coloured symbols). OCs located at $R_G \lesssim 7$ kpc are subject to a stronger external gravitational field, which might explain their more compact external structures.

6 SUMMARY AND CONCLUDING REMARKS

In this paper, we revisited the cases of 14 objects previously classified as low-contrast or faint Galactic OCs. In general, these OCs are projected against a dense stellar background, because

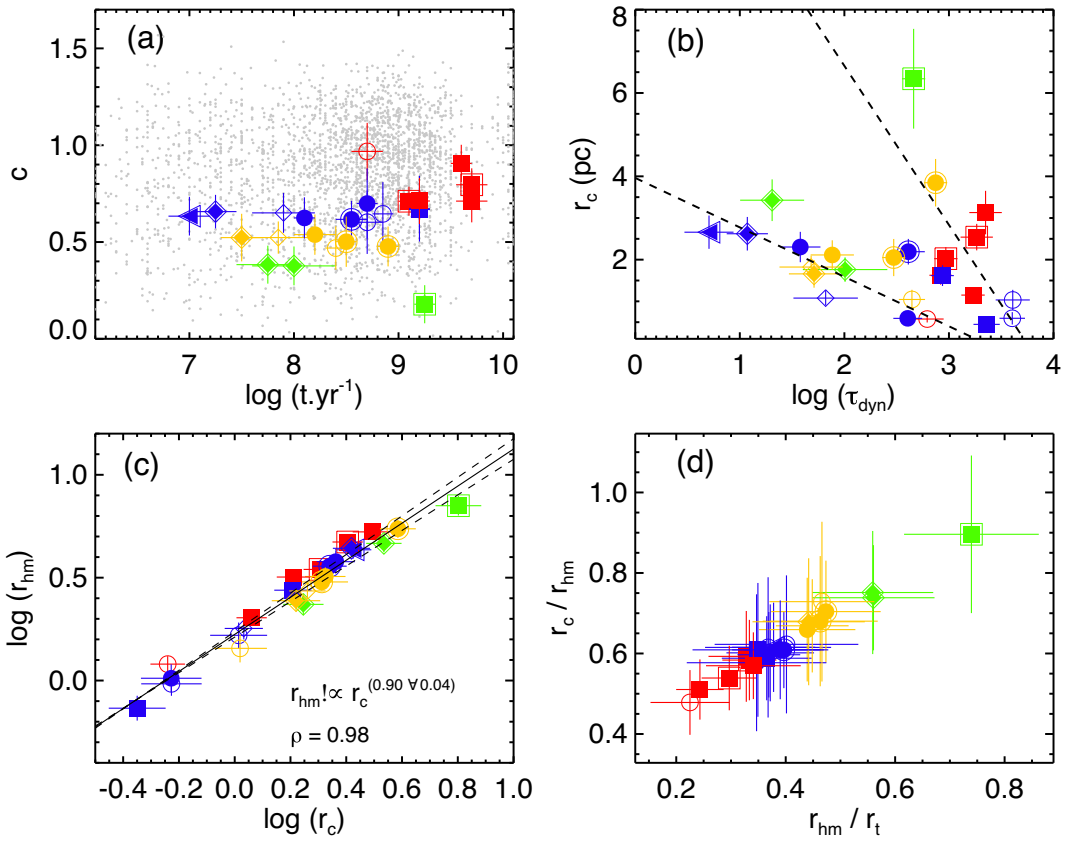

Figure 14. (a) Concentration parameter c versus age plot. Symbol colours were given according to the c intervals shown in Table 3. The grey dots represent clusters in the sample of Kharchenko et al. (2013). (b) r_c versus logarithmic dynamical ratio (τ_{dyn}). The two dashed lines suggest different evolutionary paths and were plotted to guide the eye. (c) r_{hm} versus r_c plot, both in log scale. The solid line is the linear fit between both radii and the dashed lines represent the fit uncertainties. (d) r_c/r_{hm} versus r_{hm}/r_t plot. The same symbol convention was employed in all panels.

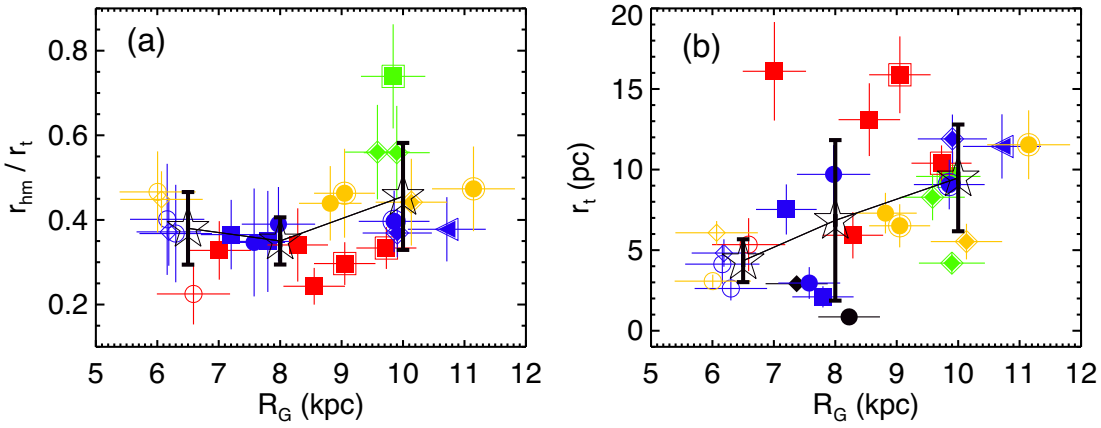

Figure 15. (a) r_{hm}/r_t ratio versus Galactocentric distance (R_G). (b) r_t versus R_G plot. The black symbols represent the OCs Lynga 2 (filled diamond) and Herschel 1 (filled circle), for which no r_c and r_{hm} could be obtained (see Table 1). The black open stars show the mean and dispersion in r_{hm}/r_t (panel a) and rt (panel b) for OCs in three R_G bins (see text for details).

of their low Galactic latitudes (typically $|b| \lesssim 5°$), and/or they present depleted evolutionary sequences, as a result of mass loss as a consequence of their dynamical evolution. Two other OCs (i.e. NGC 2421 and [FSR2007] 1325) were included in the main sample, as they are projected in the same fields of Czernik 31 and Czernik 32. In fact, our results suggest that Czernik 31 and NGC 2421 form a physical binary, as inferred from their compatible distances, colour excesses and RDPs. The dynamics of this probable pair could be better investigated with the determination of radial velocities. In turn, the apparent proximity between Czernik 32 and [FSR2007] 1325 seems just a projection effect, as these two clusters present distances and colour excesses that are incompatible with the hypothesis of a pair of interacting OCs. For comparison purposes, we also investigated a complementary sample of 11 OCs, which

are more readily distinguishable from the general Galactic disc population.

For each cluster, our analysis procedure was divided into three basic steps. (i) A pre-analysis procedure, during which the applying of dedicated magnitude filters on the cluster CMD and the inspection of its VPD allowed us to check preliminarly its physical existence; at this stage, a proper motion filter was also applied in order to alleviate the contamination by field stars. (ii) Determination of structural parameters from the cluster RDP by minimization of χ^2 while fitting King (1962) and Plummer (1911) profiles. (iii) Selection of member stars, at which stage, the magnitude filter was dismissed and we searched for stars with high membership likelihoods in the region $r \leq r_t$; these stars define clear evolutionary sequences in decontaminated $G \times (G_{BP} - G_{RP})$ CMDs.

All investigated objects had their physical nature confirmed as genuine OCs, contrary to studies that pointed out the presence of some asterisms, which were the cases of Ruprecht 30 and NGC 3519. In the case of Ruprecht 130, no firm conclusions could be drawn by previous studies regarding its physical nature. Our results point out a real physical system. Mean astrometric parameters derived here are in close agreement with recent studies based on *Gaia* DR2. Despite this, the fundamental astrophysical parameters $E(B - V)$, $(m - M)_0$ and $\log(t)$ present important discrepancies with the literature, most probably because of different procedures for the selection of member stars. Because our method is based on high-precision astrometry and photometry, we could obtain deeper CMDs and more refined lists of members.

Our investigated OCs are located between or close to the Sagittarius and Perseus spiral arms (R_G ~6−11 kpc), spanning a wide range of ages ($\log t \sim 7.0$−9.7) and evolutionary stages. Most of them present solar metallic content. The joint analysis of our complete sample suggests a general scenario in which, as clusters evolve dynamically and gradually lose stars (preferentially lower-mass stars) by evaporation, their overall structure becomes more compact. This can be inferred from the negative correlation between r_c and the dynamical ratio (τ_{dyn}); that is, more centrally concentrated clusters tend to be more dynamically evolved. The trends exhibited in the r_c versus τ_{dyn} plot suggest two distinct evolutionary sequences, which may be consequence of different initial conditions at formation. From the positive correlation between r_c/r_{hm} and r_{hm}/r_t ratios, we can see that in fact more compact OCs are less tidally filled and thus less subject to a larger mass loss due to tidal effects. In this scenario, for a given set of initial formation conditions, the OC dynamical evolution is ruled by internal two-body relaxation, regulated by the external tidal field.

The degree of tidal filling, as measured by the r_{hm}/r_t ratio, does not exhibit a clear correlation with R_G, but this ratio presents smaller dispersion for OCs closer to the Galactic Centre. Because these structures are subject to a stronger Galactic gravitational pull, their smaller r_{hm}/r_t values favour their survival against tidal disruption. The external structure of OCs seems differentially affected by changes in the external gravitational potential: for those located at smaller R_G, their tidal r_t are smaller and with less dispersion compared with those at larger R_G.

The availability and spatial coverage of data in the *Gaia* DR2 catalogue, combined with analysis methods such as those proposed in the present paper, allows uniform and refined characterizations of an increasingly large number of clusters. This is an essential step towards a deeper understanding of the Galactic structure and its evolution, as well as to a better comprehension of the process of cluster disruption.

ACKNOWLEDGEMENTS

We thank the anonymous referee for helpful suggestions. This research has made use of the VizieR catalogue access tool, CDS, Strasbourg, France. This work has made use of data from the European Space Agency (ESA) mission *Gaia* (https://www.cosmos.esa.int/gaia), processed by the *Gaia* Data Processing and Analysis Consortium (DPAC; https://www.cosmos.esa.int/web/gaia/dpac/consortium). Funding for the DPAC has been provided by national institutions, in particular the institutions participating in the *Gaia* Multilateral Agreement. This research has made use of *Aladin sky atlas* developed at CDS, Strasbourg Observatory, France. The authors thank the Brazilian financial agencies CNPq and FAPEMIG. This study was financed in part by the Coordenação de Aperfeiçoamento de Pessoal de Nível Superior − Brazil (CAPES) − Finance Code 001.

REFERENCES

Angelo M. S., Santos J. F. C., Corradi W. J. B., Maia F. F. S., 2019a, A&A, 624, A8
Angelo M. S., Piatti A. E., Dias W. S., Maia F. F. S., 2019b, MNRAS, 488, 1635
Arenou F. et al., 2018, A&A, 616, A17
Baumgardt H., Parmentier G., Gieles M., Vesperini E., 2010, MNRAS, 401, 1832
Bianchin M., Lima E. F., Bica E., Riffel R. A., Bonatto C., Saito R. K., 2019, PASA, 36, e044
Bica E., Bonatto C., 2005, A&A, 443, 465
Bica E., Bonatto C., 2011, A&A, 530, A32
Bica E., Bonatto C., Blumberg R., 2006, A&A, 460, 83
Bica E., Pavani D. B., Bonatto C. J., Lima E. F., 2019, AJ, 157, 12
Bonatto C., Bica E., 2007, MNRAS, 377, 1301
Bonatto C., Bica E., Pavani D. B., 2004, A&A, 427, 485
Bonfanti A., Ortolani S., Nascimbeni V., 2016, A&A, 585, A5
Bressan A., Marigo P., Girardi L., Salasnich B., Dal Cero C., Rubele S., Nanni A., 2012, MNRAS, 427, 127
Brown A. G. A.Gaia Collaboration et al. (Gaia Collaboration), 2018, A&A, 616, A1
Cantat-Gaudin T. et al., 2018a, A&A, 615, A49
Cantat-Gaudin T. et al., 2018b, A&A, 618, A93
Carraro G., Vázquez R. A., Costa E., Perren G., Moitinho A., 2010, ApJ, 718, 683
Castro-Ginard A., Jordi C., Luri X., Julbe F., Morvan M., Balaguer-Núñez L., Cantat-Gaudin T., 2018, A&A, 618, A59
Chen B. et al., 2001, ApJ, 553, 184
Cheon S., Sung H., Bessell M. S., 2010, Journal of Korean Astronomical Society, 43, 115
Cutri R. M. et al., 2012, VizieR Online Data Catalog, 2311
de La Fuente Marcos R., 1996, A&A, 314, 453
de La Fuente Marcos R., 1997, A&A, 322, 764
de La Fuente Marcos R., de La Fuente Marcos C., 2009, A&A, 500, L13
Dias W. S., Alessi B. S., Moitinho A., Lépine J. R. D., 2002, A&A, 389, 871
Dias W. S., Monteiro H., Lépine J. R. D., Prates R., Gneiding C. D., Sacchi M., 2018, MNRAS, 481, 3887
Dias W. S., Monteiro H., Lépine J. R. D., Barros D. A., 2019, MNRAS, 486, 5726
Ferraro F. R., Lanzoni B., Dalessandro E., Cadelano M., Raso S., Mucciarelli A., Beccari G., Pallanca C., 2019, Nature Astronomy, 3, 1149
Ferreira F. A., Santos J. F. C., Corradi W. J. B., Maia F. F. S., Angelo M. S., 2019, MNRAS, 483, 5508
Froebrich D., Scholz A., Raftery C. L., 2007, MNRAS, 374, 399
Katz D.Gaia Collaboration et al. (Gaia Collaboration), 2018, A&A, 616, A11

Heggie D. C., 1975, MNRAS, 173, 729
Hills J. G., 1975, AJ, 80, 809
Hut P., Bahcall J. N., 1983, ApJ, 268, 319
Innanen K. A., Wright A. E., House F. C., Keenan D., 1972, MNRAS, 160, 249
Kharchenko N. V., Piskunov A. E., Schilbach E., Röser S., Scholz R.-D., 2013, A&A, 558, A53
King I., 1962, AJ, 67, 471
Krone-Martins A., Moitinho A., 2014, A&A, 561, A57
Lawrence A. et al., 2007, MNRAS, 379, 1599
Luri X. et al., 2018, A&A, 616, A9
Mackey A. D., Wilkinson M. I., Davies M. B., Gilmore G. F., 2008, MNRAS, 386, 65
Maia F. F. S., Corradi W. J. B., Santos J. F. C., Jr, 2010, MNRAS, 407, 1875
Minniti D. et al., 2010, New Astron., 15, 433
Monteiro H., Dias W. S., 2019, MNRAS, 487, 2385
Netopil M., Paunzen E., Stütz C., 2012, Astrophysics and Space Science Proceedings, 29, 53
Netopil M., Paunzen E., Heiter U., Soubiran C., 2016, A&A, 585, A150
Ostriker J. P., Spitzer Lyman J., Chevalier R. A., 1972, ApJ, 176, L51
Pavani D. B., Kerber L. O., Bica E., Maciel W. J., 2011, MNRAS, 412, 1611
Perren G. I., Vázquez R. A., Piatti A. E., 2015, A&A, 576, A6
Piatti A. E., Dias W. S., Sampedro L. M., 2017, MNRAS, 466, 392
Piskunov A. E., Schilbach E., Kharchenko N. V., Röser S., Scholz R.-D., 2007, A&A, 468, 151
Plummer H. C., 1911, MNRAS, 71, 460
Portegies Zwart S. F., McMillan S. L. W., Hut P., Makino J., 2001, MNRAS, 321, 199
Portegies Zwart S. F., McMillan S. L. W., Gieles M., 2010, ARA&A, 48, 431
Reid M. J., 1993, ARA&A, 31, 345
Reina-Campos M., Kruijssen J. M. D., Pfeffer J. L., Bastian N., Crain R. A., 2019, MNRAS, 486, 5838
Roeser S., Demleitner M., Schilbach E., 2010, AJ, 139, 2440
Rossi L. J., Bekki K., Hurley J. R., 2016, MNRAS, 462, 2861
Sagar R., Bhatt H. C., 1989, MNRAS, 236, 865
Skrutskie M. F. et al., 2006, AJ, 131, 1163
Spitzer L., Jr, 1958, ApJ, 127, 17
Theuns T., 1991, Mem. Soc. Astron. Italiana, 62, 909
Vallée J. P., 2008, AJ, 135, 1301
van Altena W. F., 2013, Astrometry for Astrophysics. Cambridge Univ. Press, Cambridge

SUPPORTING INFORMATION

Supplementary data are available at *MNRAS* online.

Please note: Oxford University Press is not responsible for the content or functionality of any supporting materials supplied by the authors. Any queries (other than missing material) should be directed to the corresponding author for the article.

This paper has been typeset from a TEX/LATEX file prepared by the author.